iScience

CellPress
OPEN ACCESS

Article

Ontogeny of cellular organization and LGR5 expression in porcine cochlea revealed using tissue clearing and 3D imaging

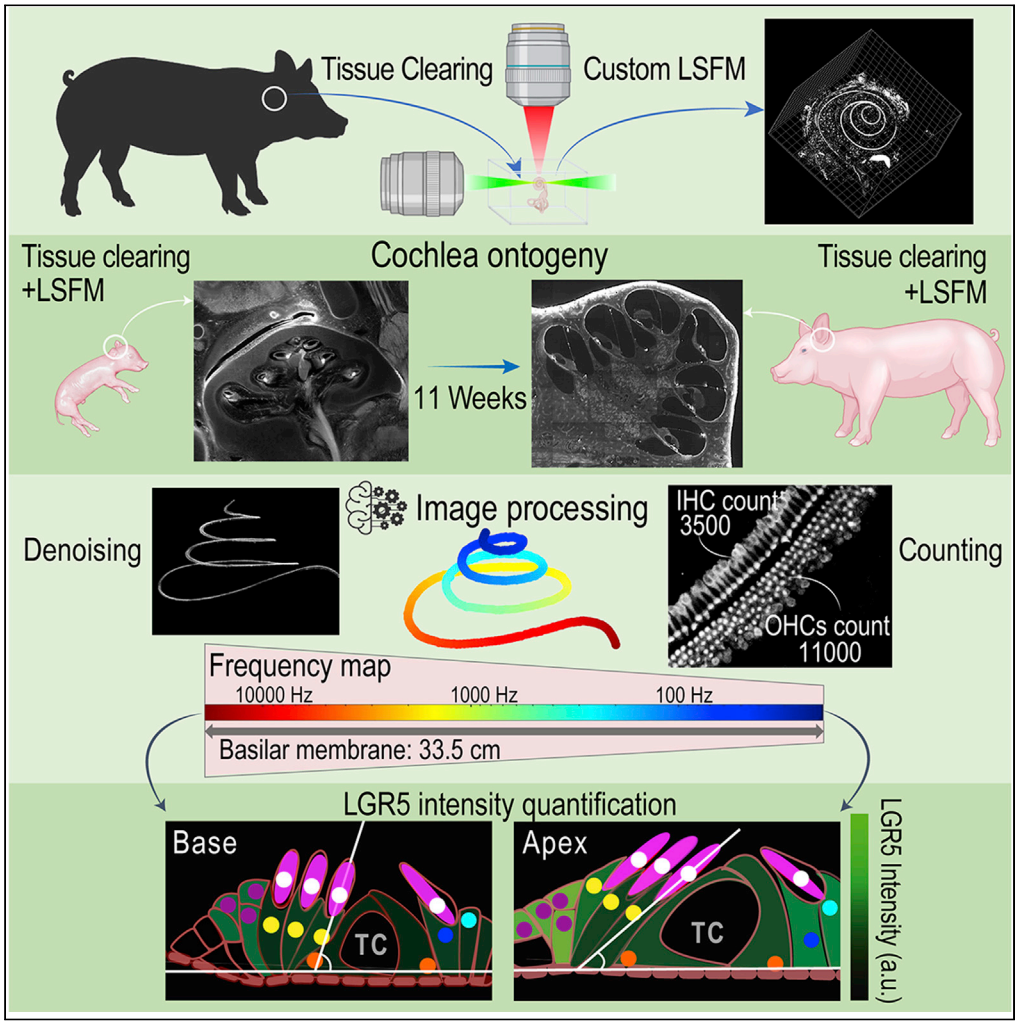

Adele Moatti, Chen Li, Sasank Sivadanam, ..., Alan G. Cheng, Frances S. Ligler, Alon Greenbaum

greenbaum@ncsu.edu

Highlights

Porcine cochlear cartography unveiled via tissue clearing and light-sheet microscopy

The porcine cochlea development rate and characteristics found to be similar to humans

The LGR5 expression in the cochlear cells in pigs was different from that in mice

The porcine cochlea showed increased relevance compared to the murine model for translational research

Moatti et al., iScience 25, 104695
August 19, 2022
https://doi.org/10.1016/j.isci.2022.104695

iScience

CellPress
OPEN ACCESS

Article

Ontogeny of cellular organization and LGR5 expression in porcine cochlea revealed using tissue clearing and 3D imaging

Adele Moatti,[1,2,5] Chen Li,[1,2] Sasank Sivadanam,[1] Yuheng Cai,[1,2] James Ranta,[3] Jorge A. Piedrahita,[1,2] Alan G. Cheng,[4] Frances S. Ligler,[1,2] and Alon Greenbaum[1,2,*]

SUMMARY

Over 11% of the world's population experience hearing loss. Although there are promising studies to restore hearing in rodent models, the size, ontogeny, genetics, and frequency range of hearing of most rodents' cochlea do not match that of humans. The porcine cochlea can bridge this gap as it shares many anatomical, physiological, and genetic similarities with its human counterpart. Here, we provide a detailed methodology to process and image the porcine cochlea in 3D using tissue clearing and light-sheet microscopy. The resulting 3D images can be employed to compare cochleae across different ages and conditions, investigate the ontogeny of cochlear cytoarchitecture, and produce quantitative expression maps of LGR5, a marker of cochlear progenitors in mice. These data reveal that hair cell organization, inner ear morphology, cellular cartography in the organ of Corti, and spatiotemporal expression of LGR5 are dynamic over developmental stages in a pattern not previously documented.

INTRODUCTION

Normal adult human hearing covers a broad frequency range (20 Hz–20k Hz) that spans deep bass to high whistling sounds (Burns et al., 1992; Purves et al., 2001). The loss of hearing at low frequency (<3,000 Hz) affects the perception of low-pitched and deeper sounds important for sound localization, while people who suffer from high-frequency hearing loss (3,000–8,000 Hz) are unable to hear high-pitched sounds such as consonants (Hornsby and Ricketts, 2006). Most rodent models that are used to study hearing loss have rather different frequency ranges from humans. An animal model that matches the human organ's size and frequency range could guide novel treatment plans in relation to therapeutic dosage, diffusion, targetability, and efficiency. The similarity in size also facilitates the analysis of conductive hearing loss where the size and structure of the middle ear is a critical factor (Kim and Koo, 2015).

The porcine model can address the above gaps. In general, the pig is an attractive translational mammalian model owing to its similarity with humans in terms of size, physiology, developmental stages, and disease progression (Lunney, 2007). The porcine model, in terms of genome evolution rate, can be positioned between non-human primates and rodents, a comparison that extends to the inner ear (Hosoya et al., 2016). In addition, porcine gene-editing tools and somatic cell nuclear transfer (SCNT) are thoroughly developed (Dai et al., 2002; Zhao et al., 2019). This is a considerable advantage as hearing loss research has benefited tremendously from the generation of gene-edited animal models (Farooq et al., 2020; Zou et al., 2015). In comparison with non-human primates, the pig is easier to breed and handle, and its use as an animal model has fewer ethical concerns.

Specifically, the pig is suitable for auditory research given its morphology, size, and hearing range. The pig, like humans and unlike most rodents, can hear at birth and has a hearing range (42 Hz–40 kHz) that overlaps better with humans (20–20 kHz) (Heffner and Heffner, 1990). The low frequency (42 Hz) is closer to that of humans (20 Hz) than for mice (~2000 Hz), Mongolian gerbils (100 Hz), or even chinchillas (50 Hz) (Engel, 2008; Heffner and Heffner, 1990, 2007; Purves et al., 2001; Ryan, 1976a; Trevino et al., 2019). Previous studies reported that the anatomy of the porcine middle ear is very similar to that of

[1]Joint Department of Biomedical Engineering, University of North Carolina at Chapel Hill and North Carolina State University, Raleigh, NC 27606, USA

[2]Comparative Medicine Institute, North Carolina State University, Raleigh, NC 27606, USA

[3]Department of Electrical Engineering, North Carolina State University, Raleigh, NC 27606, USA

[4]Department of Otolaryngology-Head and Neck Surgery, Stanford University School of Medicine, Stanford, CA 94305, USA

[5]Lead contact

*Correspondence: greenbaum@ncsu.edu

https://doi.org/10.1016/j.isci.2022.104695

humans (Gurr et al., 2009). Additionally, the morphology of the cochlear hair cells, their organization and distribution (Guo et al., 2015), and the maturity of the porcine auditory system at birth (Lovell and Harper, 2007) are similar to humans. The porcine model could be an excellent model system both for genetic and noise-induced hearing loss. For example, several recent reports used transgenic porcine models to study deafness and explore the applicability of gene therapy for rare genetic diseases that cause hearing loss—e.g., Waardenburg syndrome (Guo and Yang, 2015; Hai et al., 2017; Xu et al., 2020). Measurements of behavior and physiological responses (i.e., auditory brainstem responses) to sounds have been established in wild-type pigs, thus providing a crucial step for creating a noise-induced hearing loss model (Anderson et al., 2019; Heffner and Heffner, 1990; Kristensen and Gimsing, 1988). However, there is still a significant gap to connect these *in-vivo* measurements and rough anatomical and mechanical studies to molecular and cellular phenomena in the porcine cochlea. The gap arises as the porcine cochlea (like human cochlea) is buried in a massive temporal bone, and it is challenging to process it for histological analysis (Knoll et al., 2019; Montgomery and Cox, 2016). The benefit of using 3D imaging such as light-sheet fluorescent microscopy (LSFM) and synchrotron radiation phase-contrast imaging has been shown previously in imaging cochlea (Hutson et al., 2021; Keppeler et al., 2021; Kopecky et al., 2012; Li et al., 2021b). Some of these seminal studies show LSFM images of the mouse, gerbil, and marmoset, which are considerably smaller than the human and porcine cochlea. We have introduced a methodology to image the porcine cochlea in 3D using tissue clearing and custom light-sheet microscopy (Moatti et al., 2020). This method maintains, with high fidelity, the 3D structure of the cochlea that is important to its proper function.

Here we also expand this methodology for 3D histology, and we investigate the ontogeny of the porcine cochlea with respect to characteristics such as basilar membrane length and hair cell count. We have also utilized the transgenic pig model in which histone 2B (H2B)-green fluorescent protein (GFP) expresses under the control of leucine-rich repeat-containing G protein-coupled receptor 5 (LGR5) promotor (LGR5-H2B-GFP) (Polkoff et al., 2020). Evidence from murine studies suggests that the $LGR5^+$ supporting cells could be progenitors of hair cells and that expansion of $LGR5^+$ cells could trigger the regeneration of hair cells in mice (Cox et al., 2014; Lenz et al., 2019; McLean et al., 2017; Shi et al., 2012; Wang et al., 2015). However, the spontaneous regeneration capability of $LGR5^+$ cells seems to disappear after the first postnatal week (Lenz et al., 2019; McLean et al., 2017), which corresponds to the maturation of the cochlea in mice. Here, we seek to generate a clear LGR5 expression map in a porcine model which could be used as a guide to evaluating the regeneration potential of $LGR5^+$ supporting cells after birth. It is important to consider that, unlike many other antibodies that we have previously tested, commercial anti-LGR5 antibodies are not reactive with porcine stem cells or with human stem cells (Tan et al., 2020); therefore, the utilization of the transgenic pig was paramount to unlock the expression patterns of these important $LGR5^+$ cells.

To characterize cellular $LGR5^+$ expression and to set the foundation for a comprehensive quantitative cochlea reference atlas, we used the 3D histology method mentioned above to reconstruct a 3D frequency map of the porcine cochlea. From this map, we could easily register (i.e., transforming different datasets into one coordinate system) and compare cochleae across different ages, as well as generate a quantitative spatiotemporal map of LGR5 in supporting cells.

Together with past porcine auditory studies, this work establishes the pig as an excellent large animal model for understanding hearing impairment, mapping cochlea development, and exploring regenerative medical therapies before translation into humans.

RESULTS

Clearing, imaging, and analysis of the porcine cochlea to derive quantitative expression maps comparable across specimens

Clearing, labeling, and imaging the mature cochleae of pigs required resection from the surrounding bone and an optimized tissue-clearing protocol. The BoneClear process was used to render the tissue transparent (Wang et al., 2019), and the 3D volume of the specimen was imaged using a custom adaptive light-sheet microscope, as described in our previous works (Li et al., 2021a; Moatti et al., 2020). The custom adaptive light-sheet microscope can provide excellent optical sectioning capabilities while maintaining a fast acquisition rate (Santi et al., 2009). The resulting 3D images were processed using the data analysis pipeline that is depicted in Figure 1A. Figure 1B shows representative images of a postnatal day 0 (P0)

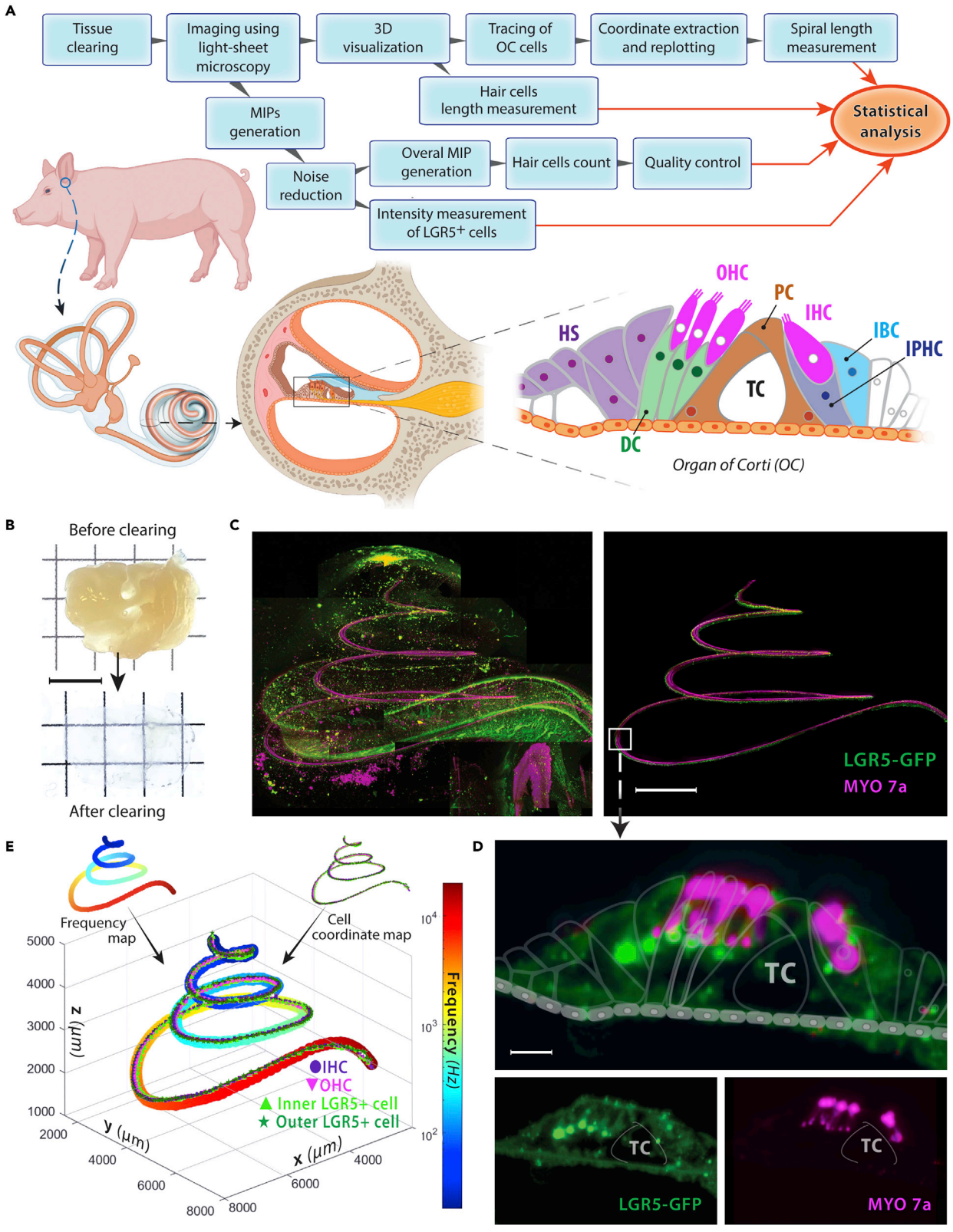
A
Tissue clearing
Imaging using light-sheet microscopy
3D visualization
Tracing of OC cells
Coordinate extraction and replotting
Spiral length measurement
Hair cells length measurement
Statistical analysis
MIPs generation
Noise reduction
Overal MIP generation
Hair cells count
Quality control
Intensity measurement of LGR5+ cells
OHC
PC
IHC
IBC
IPHC
HS
TC
DC
Organ of Corti (OC)
B
Before clearing
After clearing
C
LGR5-GFP
MYO 7a
D
TC
TC
LGR5-GFP
TC
MYO 7a
E
Frequency map
Cell coordinate map
IHC
OHC
Inner LGR5+ cell
Outer LGR5+ cell
z (μm)
y (μm)
x (μm)
Frequency (Hz)

Figure 1. Clearing, imaging, and analyses of porcine cochleae

(A) A block diagram outlining the key steps of sample preparation, imaging, and computational pipeline that uses 3D visualization and analysis. The schematic illustration depicts the porcine cochlea and organ of Corti; tunnel of Corti: TC, organ of Corti: OC, inner hair cell: IHC, outer hair cell: OHC, inner border cell: IBC, inner phalangeal cell: IPHC, pillar cells: PC, Deiters cell: DC, and Hensen cell: HS.

(B) A cochlea of a newborn pig before and after tissue clearing. Scale bar, 0.5 cm.

(C) Maximum intensity projection (MIP) image with radial view orientation of a transgenic porcine cochlea (P120; LGR5-H2B-GFP) before and after noise reduction. Scale bar, 1000 μm.

(D) The zoom-in digital section where the white boxed region in (C) resides (5 μm thick). The sample was stained for MYO7a (hair cells; magenta) and GFP ($LGR5^+$ cells; green). Scale bar, 50 μm.

(E) An overlay 3D frequency-cellular map. Overlaying the 3D frequency map with cellular coordinates allows comparison between different samples and ages. Inner and outer $LGR5^+$ cells relate to cells on either the inner or outer side of the tunnel of Corti, respectively.

cochlea before and after clearing, and it is evident that the sample was transparent after the clearing process. Figure 1C shows an example of a 3D image of a mature P120 cochlea acquired with our adaptive custom-built light-sheet microscope, and after digitally extracting the organ of Corti (OC). Radial view and zoomed-in images are shown in Figure 1D. The digital extraction removed considerable background noise and facilitated the quantitative analysis. In every sample that we imaged, hair cells were stained for MYO7a to provide a reference for the orientation and location of structures along the organ of Corti. The autofluorescence of the tissue also revealed important structural landmarks such as the tunnel of Corti, the tectorial membrane, and in some cases the neuronal cell bodies of the spiral ganglion. The 3D rendering of samples facilitated the extraction of invaluable information regarding the porcine cochlea, including measurements of the length of the spiral, length and count of hair cells, the 3D location of the cells with respect to each other, the estimated 3D-location map based on the Greenwood equation (Greenwood, 1990), and more.

The estimated 3D frequency map enabled us to register cochleae that were extracted from different animals and across different ages. In general, the frequency map correlated the position of the hair cells within the organ of Corti to a specific auditory frequency responsivity. To extract the frequency map, we traced the 3D spiral trajectory indicated by the rows of both the inner and outer hair cells and recorded the trajectory coordinates from the apex to the base. Then, using the Greenwood equation (Greenwood, 1990), the estimated 3D frequency map of the cochlea was extracted as shown in Figure 1E. We used the experimental auditory brainstem response to find low- and high-frequency limits (Heffner and Heffner, 1990). The estimated frequency map can be used as a global coordinate system to compare cochlear cytoarchitecture and protein expression across different ages and animals, for instance, LGR5 expression in the porcine supporting cells (Figure 1E).

Structural investigation of the porcine cochlea (E38 - P120) revealed that the pig cochlea is mature at birth

Using the technology described in Figure 1 and intending to use the pig as a large animal model for hearing research, we first established the developmental timeline of the porcine cochlea in comparison to humans and other established animal models. For this purpose, we examined the cochlear structure at six different time points (embryonic day 38 (E38), E53, E80, E115/Postnatal day 0 (P0), P60, and P120; Figure 2). In E38 embryos (out of 115 gestation days), the otic capsule had already formed, and the three turns of the cochlea were clearly observed (Figure 2A). In E53, the cochlear duct had lengthened, and the apical, middle, and basal turns were recognized (Figure 2B). The formation of the scala vestibuli and scala tympani, however, was incomplete; these structures were visible in the basal turn, but not in the apical or middle turn. The Reissner's membrane (RM) in the basal turn had begun to form. In the scala media, the sensory epithelium formation was still immature (Figure S1A). This stage resembles E15.5 in mice (Kopecky et al., 2012).

In the human fetal cochlea, the anatomical maturation of the scala tympani and scala vestibuli occurs up to gestation week 17 (GW17) (Kim et al., 2011; Locher et al., 2013), and by GW20, the stria vascularis has developed. In E80 embryos of the pig, like GW20 in humans, P9 in mice, and P12 in rats (Kim et al., 2011; Locher et al., 2013; Roth and Bruns, 1992), the cochlear duct was well developed, comprising 3.5 turns (Figure 2C); the scala vestibuli, scala tympani, and scala media were fully developed, as pointed out by arrows in Figure 2C. In the scala media, the sensory epithelium, the organ of Corti, and stria vascularis (StV) formation appeared more mature (Figure 2C). However, we identified that the height and width of the tunnel of Corti (TC) at E80 were significantly smaller than in older cochlea using a two-way ANOVA (Figure S1B). In the

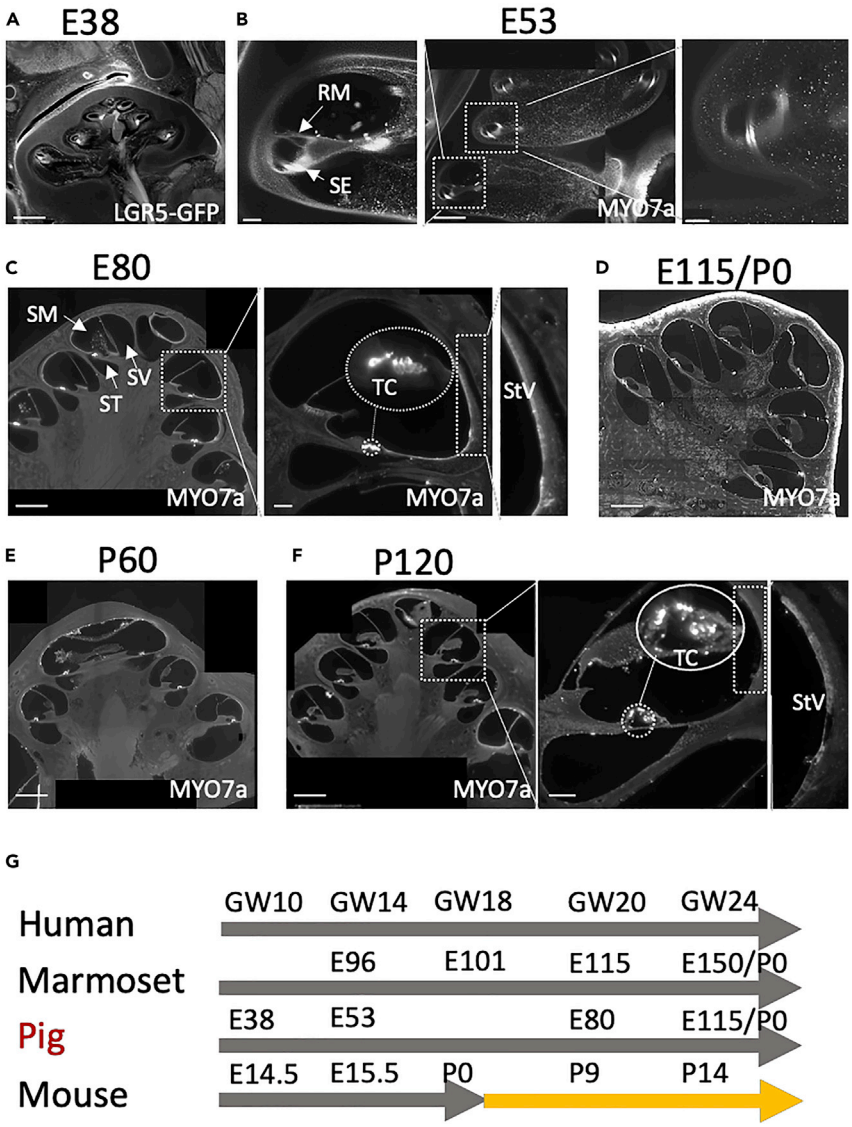

Figure 2. Developmental stages of the porcine cochlea

In all the images the autofluorescence revealed the overall cochlear morphology, while the specific markers provided information about the cellular organization.

(A) A radial view of the porcine cochlea duct in a **day 38 embryo** (LGR5-GFP staining). At this stage, the Otic Capsule has formed, and the 3 turns of the cochlea are identifiable. Scale bar, 500 μm.

(B) On **day 53 of the embryo** (MYO7a staining), the cochlear duct lengthened. The formation of the scala vestibuli and scala tympani was incomplete. Scale bar, 500 μm; in zoom-in images, 100 μm. The sensory epithelium (SE) at this age is immature (See Figure S1). The Reissner's membrane (RM) in the basal turn began to form.

(C) On **day 80 of the embryo** (MYO7a staining), the cochlear duct is well developed, with the arrows pointing towards a developed scala vestibuli (SV), scala tympani (ST), and scala media (SM). The tunnel of Corti (TC) and Stria Vascularis (StV) formation is relatively mature. Scale bar, 500 μm; in zoom-in images, 100 μm.

(D–F) On postnatal **day 0**, postnatal **day 60**, and postnatal **day 120**, the cochlea (MYO7a staining) is morphologically mature. We also observed that the height of the Tunnel of Corti increases in a basal-to-apex gradient (MYO7a) (See Figure S1). Scale bar, 500 μm; in zoom-in images, 100 μm.

(G) The equivalent gestation period of the pig in comparison to the human, marmoset, and mouse is presented (Basch et al., 2016; Hosoya et al., 2021; Igarashi and Ishii, 1980; Kim et al., 2011; Locher et al., 2013; Cantos et al., 2000; Roccio and Edge, 2019). The yellow arrow denotes equivalent postnatal development in mice. Scale bar, 500 μm.

lesser epithelial ridge (LER), outer sulcus cells, Claudius cells, and HS were well-formed at this stage (Figures 2C and S1C). However, in the greater epithelial ridge (GER) on the neural side, cells only partially regressed and still developing into inner sulcus cells in the apex. This is in accordance with what has been reported before with cochlea maturation from base to apex (Rubel, 1984).

At postnatal day 0, the cochlear formation was completed (Figure 2D), including full regression of Kölliker's organ and increased height and width of the TC that was not observed for E80 (Figures 2D and S1B). In a mature cochlea (Figures 2D–2F; P0, P60, and P120, respectively), we observed the stria vascularis comprising all three layers: marginal cells, intermediate cells, and basal cells (Figure S1D). The equivalent gestation period of the pig in comparison to a human, a common marmoset, and a mouse is also provided in Figure 2G (Basch et al., 2016; Hosoya et al., 2021; Igarashi and Ishii, 1980; Kim et al., 2011; Locher et al., 2013; Cantos et al., 2000; Roccio and Edge, 2019). We did not observe any major macroscopic structural changes between P0 and P120 cochleae.

Organ of Corti cartography and changes in hair cell morphology and organization along the basilar membrane

After establishing the cochlea developmental timeline in pigs, we examined whether the hair cells change their morphology and organization across ages and cell location in the organ of Corti along the basilar membrane. To compare different samples and ages, we first examined the length of the basilar membrane as a function of age. We expected that the length would remain constant, as the pig cochlea is fully lengthened at E80 and no significant changes were observed between E80, P0, P60, and P120. The length of cochlear spirals was calculated for E80 (N = 4), P0 (N = 15), P60 (N = 4), and P120 (N = 11) cochleae after tracing the basilar membrane. The tracing was performed based on the locations of the inner and outer hair cells (IHC, OHC), and the results are displayed in Figure 3A. The average length of the basilar membrane is 33,000 $\pm$ 500 μm (mean $\pm$ SD) from IHC tracing and 34,000 $\pm$ 500 μm from OHC tracing. There were no significant differences in the basilar membrane length between ages using a one-way ANOVA test. Statistical analysis of spiral length in P0 cochleae showed no significant differences between males and females, with the caveat that fewer female cochleae were available for analysis (Figure S2A). Figure 3B depicts the cochlear length across different species (West, 1985; Fay, 2012; Békésy et al., 1990; Greenwood, 1990; Heffner and Heffner, 1985, 1990, 1991; Heffner and Masterton, 1980; Heffner et al., 1971, 1971; Lovell and Harper, 2007; Manoussaki et al., 2008; Ryan, 1976b). Interestingly, the cochlear length of pigs was found to be the same as humans. We have also established the number of inner hair cells and outer hair cells for P0 (N = 12) porcine cochleae and counted them to be 3,200 $\pm$ 300 and 11,500 $\pm$ 1,600 (mean $\pm$ SD), respectively, as shown in Figure 3C. These numbers are strikingly similar to humans (3,500 IHC and 11,000–12,000 OHC) (Ashmore, 2008). We did not observe any significant differences in hair cell numbers between the sexes.

Next, we investigated hair cell morphology and organization across ages and cell location in the organ of Corti. To this end, we performed a comparison of the hair cell organization at six specific frequencies $\approx$40, 100, 700, 2,000, 10,000, and 20,000 Hz corresponding to 0, 0.03, 0.2, 0.37, 0.68, and 0.82 locations along the spiral, respectively, if the apex is 0 and the base is 1, as shown in Figure S2B. These locations were marked on the reconstructed 3D image of a representative cochlea depicted in Figure 3D. The comparison based on frequencies in earlier developmental ages than E80 can be inaccurate owing to the fact that the cochlea might be undergoing non-uniform expansion. At the apex of the E80 cochlea, the IHC and OHC rows are very close to each other without any noticeable gap between them, suggesting a very narrow or nonexistent tunnel of Corti. The tunnel of Corti was more apparent towards the middle and base of the cochlea. Across all ages, we observed OHC disorganization in frequencies below 700 Hz, and in some cases, OHCs deviated from the hallmark three-row structures (having one or two rows) that are observed at higher frequencies. To provide more details regarding OHC disorganization at the apex, 6 different frequencies below 700 Hz were selected and depicted in Figure S2C. The OHC disorganization at 40 and 100 Hz persisted at older ages, e.g., P120 mature cochleae, even though older cochleae are relatively more organized than younger cochleae. Altogether, we postulate that the organization of OHCs in the apex represents the last step in the cochlear maturation as reported for other animal models (Rubel, 1984) and varies between animals of the same age. Other than the disorganization of the OHC at lower frequencies, we also observed lengthier outer hair cells in that region. As the hair cell length increases, the cells tend to tilt more, and the incline is more apparent at lower frequencies than at higher frequencies (Videos S1, S2,and S3) which will be discussed in the next section.

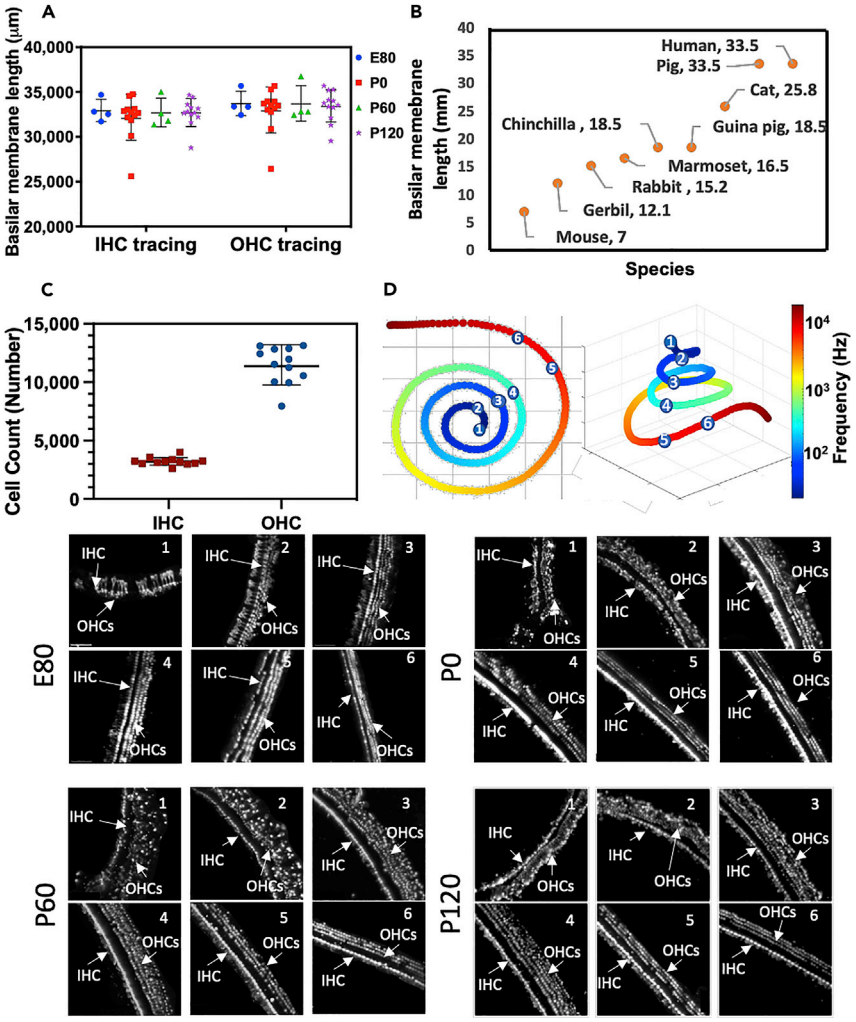

Figure 3. The organ of Corti morphology is frequency specific

(A) The basilar membrane lengths of E80 (N = 4), P0 (N = 15), P60 (N = 4), and P120 (N = 11) cochleae (mean ± SD) were measured using IMARIS for both the inner and outer hair cells (IHC, OHC) spiral trajectory.

(B) The basilar membrane length across different species is presented (West, 1985; Fay, 2012; Békésy et al., 1990; Greenwood, 1990; Heffner and Heffner, 1985, 1990, 1991; Heffner and Masterton, 1980; Heffner et al., 1971, 1971; Lovell and Harper, 2007; Manoussaki et al., 2008; Ryan, 1976b; Johnson et al., 2012); the pigs spiral length is the same as humans.

(C) The inner and outer hair cells numbers were counted for P0 (N = 12) cochleae (mean ± SD), and their numbers are very similar to humans.

(D) A comparison of hair cell organization as a function of age and estimated auditory frequency is illustrated at (1) 40 Hz, (2) 100 Hz, (3) 700 Hz, (4) 2 kHz, (5) 10 kHz, and (6) 20 kHz related to 0, 0.03, 0.2, 0.37, 0.68, and 0.82 location along the spiral, respectively, if the apex is 0 and the base is 1. At low frequencies (e.g., 40 and 100 Hz) the hair cells are disorganized compared to higher frequencies. Scale bar, 50 μm (See Figure S2 and Videos S1, S2, and S3).

Outer hair cell elongation at low frequencies correlated with drastic changes in the organ of Corti's morphology

We measured the length of the hair cells at six specific frequencies and reported the results in Figure 4. Figure 4A shows OHC length at three representative frequencies (100, 2,000, and 10,000 Hz) out of six frequencies that were measured. The OHC length clearly changes as a function of frequency. It is reported previously in rats that before maturation, OHCs have an almost constant size along the whole cochlear duct, but as they mature, OHCs shorten at the base and elongate at the apex (Roth and Bruns, 1992). To quantify these differences, we used both the traditional approach of using 2D images, as well as a novel one using our 3D images to calculate the length of hair cells (Figures S2D and S4B, respectively). We

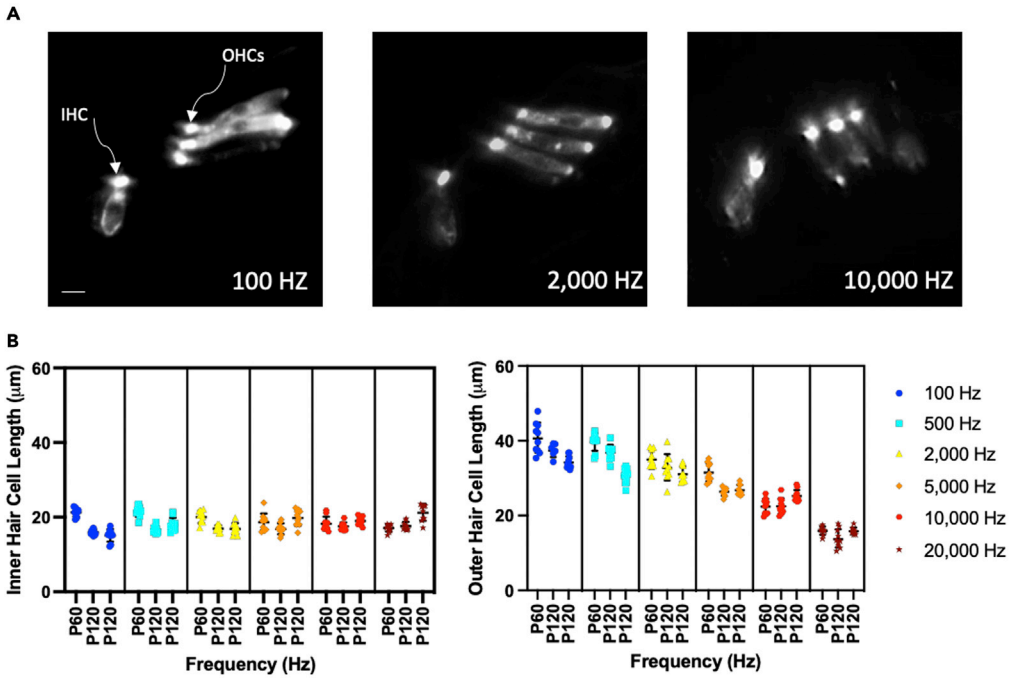

Figure 4. Hair cell length measurement in 3D images

(A) Digital slices (2 μm thickness) of hair cells (MYO7a staining) at 100 Hz, 2,000 Hz, and 10,000 Hz. The outer hair cells exhibit variable lengths. The images are from P0 porcine cochlea. Scale bar, 10 μm.

(B) The measurement of hair cell length using 3D images. The inner and outer hair cells' lengths are shown as mean ± SD (number of animals, N = 3, P60, and P120). Using 3D images allows us to capture the extent of the outer hair cells across multiple slices leading to less variability. (Video S4 shows how we measured the length of each hair cell across multiple z-planes. See Figure S2).

used 2D projection images similar to traditional 2D slides to be able to compare our measured cellular length values with literature values for other animals and report if there is any benefit to using 3D images. We simulated the single slide immunohistochemistry method to measure OHC length by using a single 5-micron section. In the 3D images, we took advantage of the multiple 5-micron z-slices across which the hair cells were extended and measured the length across multiple z-planes. Video S4 shows the procedure of measuring a hair cell's length using 3D images in IMARIS. When comparing the results of length measurement using 2D and 3D images, it was evident that using 3D images decreased the variability in length, especially at low frequencies by half (SD from ~8 to 4 μm). This comparison is in line with previous 2D measurements (SD > 8 μm or more) (Pujol et al., 1992; Zetes et al. 2012). Using the 3D images, the OHC length at 500 Hz was 37.5 ± 4.0 μm, decreasing to 15.2 ± 1.8 μm at 20,000 Hz—which was shorter than what was expected (~50 μm to ~25 μm, respectively) from previous frequency-length reports across different species including cat, mouse, rat, hamster, bat, mole-rat, guinea pig, and human (Pujol et al., 1992). Part of this difference can possibly be attributed to the slight shrinkage of the soft tissue during the clearing process (Luong et al., 2021). The IHC length remains constant at ~18 μm along the cochlear duct and across all ages. The differences in length of IHC and OHC are correlated to their different roles (Spoendlin et al., 1970). As previously shown in other tissues (Molbay et al., 2021; Neckel et al., 2016), our measurements highlight the benefits of using 3D imaging techniques in terms of preserving the cytoarchitecture better than sectioning and provide insights on the importance of using animal models with lower frequency hearing than rodents to mimic human anatomy.

Given the elongation of the OHC at low frequencies, we suspected that the position of the supporting cells might change accordingly with frequency. Therefore, we mapped the relative position of the supporting cells with respect to the inner and outer hair cells and the structural morphology at several frequencies along the cochlea. As the organ of Corti is not heavily populated with cells (Engström et al., 1964), we achieved this goal by staining the cochlea with ToPro3 (nuclear stain) and anti-MYO7a (hair cell marker). Figure 5A shows the staining results at different positions across the cochlea of a P0 pig; a schematic of

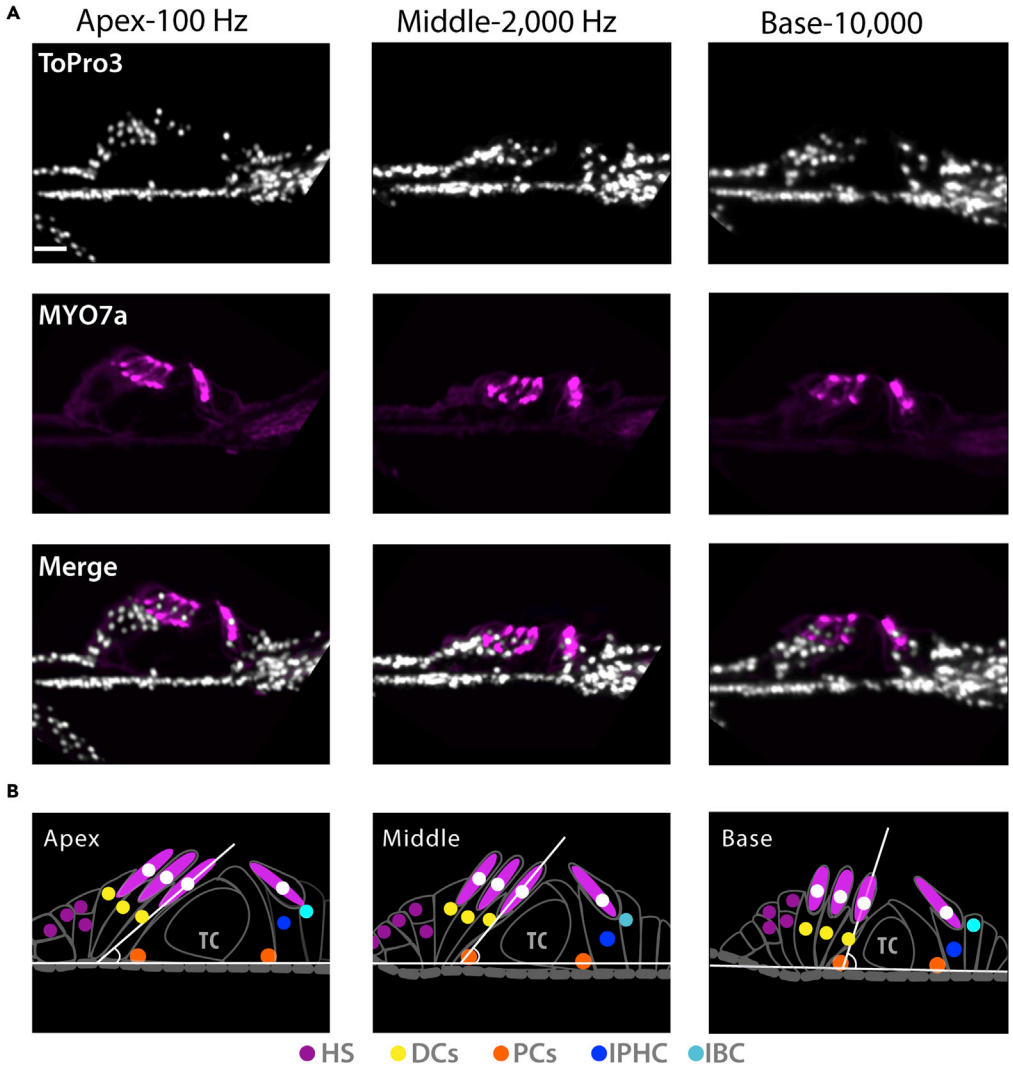

Figure 5. The organ of Corti cartography and the relative position of the supporting cells with respect to the inner and outer hair cells

(A) Anti-MYO7a antibody (hair cells) and ToPro3 (nuclear stain) are used to establish the supporting cell organization in the Organ of Corti. Three representative areas in the P0 cochlea are shown at the apex (100 Hz), middle (2,000 Hz), and base (10,000 Hz). The tunnel of Corti is used to learn the position of the pillar cells. Scale bar, 30 μm.

(B) Based on multiple porcine cochleae and the representative figures presented in (A), schematic models of cell organization in the organ of Corti are constructed for the apical, middle, and basal turns (See Figures S3–S5). The inner border cells (IBC), inner phalangeal cells (IPHC), inner and outer pillar cells (PCs), 1st, 2nd, and 3rd Deiters' cells (DCs), and Hensen cells (HS).

the cell's position is established and shown for different frequencies in Figure 5B after investigating multiple porcine cochleae of different ages. It was evident that in low frequencies (~100 Hz), where the hair cell length was almost double that at the base, the orientation of the hair cells (HC) and the adjacent Deiters' cells (DC) gradually shifted from almost perpendicular to the basilar membrane at the base (~10,000 Hz) to a 30-45-degree angle relative to the basilar membrane, Figure 5B. Similarly, previously in guinea pigs, the angle between the outer pillar cells and the basilar membrane was reported to increase toward the base of the cochlea (Zetes et al., 2012). These patterns were repeatable across all samples that we imaged and informed our cell assignments described in the following sections. The assignments were in accordance with the published 2D immunohistology in porcine cochleae (Rask-Andersen et al., 2010), confirming that the cell locations were preserved and not affected by the clearing procedure.

Quantitative LGR5 expression maps in supporting cells revealed dependency along the basilar membrane

LGR5-encoded protein is a transmembrane receptor that is involved in the Wnt signaling pathway (Haegebarth and Clevers, 2009). The Wnt signaling pathway participates in stem cell renewal, cell proliferation, and cell differentiation—both in embryogenesis and in injury repair (Ring et al., 2014). During embryogenesis, LGR5 displays a complex and elevated expression pattern, and after birth LGR5 expression in most tissues declines (Barker et al., 2012; Kinzel et al., 2014; Seishima et al., 2019; Fernandez Vallone et al., 2020). As such, cells that strongly express LGR5 in adult tissue are of particular interest in regard to tissue regeneration (Wang et al., 2015). In the mouse inner ear, it has been shown that $LGR5^{+}$ cells regenerate hair cells in the utricle via mitosis and direct trans-differentiation (Wang et al., 2015).

Given the importance of the LGR5 gene as a marker for progenitors of hair cells, we quantified LGR5 expression along the cochlea (initially we will discuss expression at P120). First, we inferred the identity of the $LGR5^{+}$ cells based on their relative position with respect to the hair cells and the tunnel of Corti (Figure 6A), building on our observations depicted in Figures 5 and S3. Using this knowledge, we assigned $LGR5^{+}$ cells to one of the supporting cell groups (Figures 6A and S3) e.g., greater epithelial ridge/inner sulcus cells (GER/ISC), inner border cells (IBC), inner phalangeal cells (IPHC), inner and outer pillar cells (IPC, OPC), 1^{st} and 2^{nd} Deiters' cells (DC12), 3^{rd} Deiters' cells (DC3), and Hensen's cells (HS) on surface view images as shown in Figure S3. Owing to the proximity of IBC to IPHC/ IPC and OPC to DC12 (and OHC at the base), there are some uncertainties in their assignment and owing to the position of OPC under DC12 (and OHC at the base) in the surface view, we do not represent OPC as a separate group.

To quantify LGR5 expression in the identified subsets of supporting cells, we measured the relative intensity of LGR5 expressing cells (GFP intensity divided by background intensity) for each supporting cell subset at six different frequencies (Figure S4). The ratio of intensities is reported in Figure 6B for P120 (n = 4). Using a nested one-way ANOVA (Table S1), we found that the supporting cells change their LGR5 expression based on cell location in the organ of Corti; this result is in line with our imaging results as evident in Figure S4 (surface view) and Figure S5 (radial view). The cochleae of all ages change their LGR5 expression based on cell location in the organ of the Corti (Table S1). Figure 6B shows that the expression at the apex was predominantly limited to IPHC, IPC, DC3, and HS, while at the base the LGR5 expression was observed mainly in the DC12, DC3, HS, and HC. To the best of our knowledge, LGR5 expression in the HS has not been reported in murine models. The expression of LGR5 in HS is of great interest and their capacity to regenerate hair cells is well-documented (Bramhall et al., 2014; Taylor et al., 2012; White et al., 2006).

Quantitative LGR5 expression maps of supporting cells revealed robust, unexpected LGR5 expression in populations such as Hensen cells (E80 – P120)

After establishing the frequency-dependent changes in LGR5 expression within mature P120 cochleae, we explored the changes in LGR5 expression with age. We compared the analysis that was conducted in Figure 6 (P120 cochleae) to additional ages (E80, P0, and P60) and the results can be seen in Figure 7. Figures 7A and 7B depict differences in the LGR5 expression pattern across ages in the apex, middle, and base. The differences in expression patterns were readily visible both quantitatively and qualitatively across ages; for instance, the expression of LGR5 in the apex and base of E80 pig was very robust compared to that in older pigs. The mixed-effect model revealed an overall significant decrease in the LGR5 intensity with the maturation of the porcine cochlea (from E80 to P120). The mixed-effect model results are summarized in Table S2. These results suggest that LGR5 expression of HS and DC3 in all ages is strong. To the best of our knowledge, the expression of LGR5 in HS has not been previously reported. At the base (frequency ~20 kHz) of the cochlea, we observed hair cells expressing LGR5 (radial view Figure S6).

DISCUSSION

We have used 3D imaging to identify morphological and structural changes during cochlear development in pigs. The advantage of using the porcine model is that it is more similar to humans than rodents in terms of hearing range, size, and gene expression. We established a method for registering different cochlea samples based on the estimated characteristic frequency at that location in the spiral; this mapping provided a function-based approach for looking at changes in cell populations along the cochlear spiral. Then, we identified changes in hair cell lengths with high precision at different estimated frequency regions of the spiral organ. Given the elongation of the hair cells in the low-frequency region,

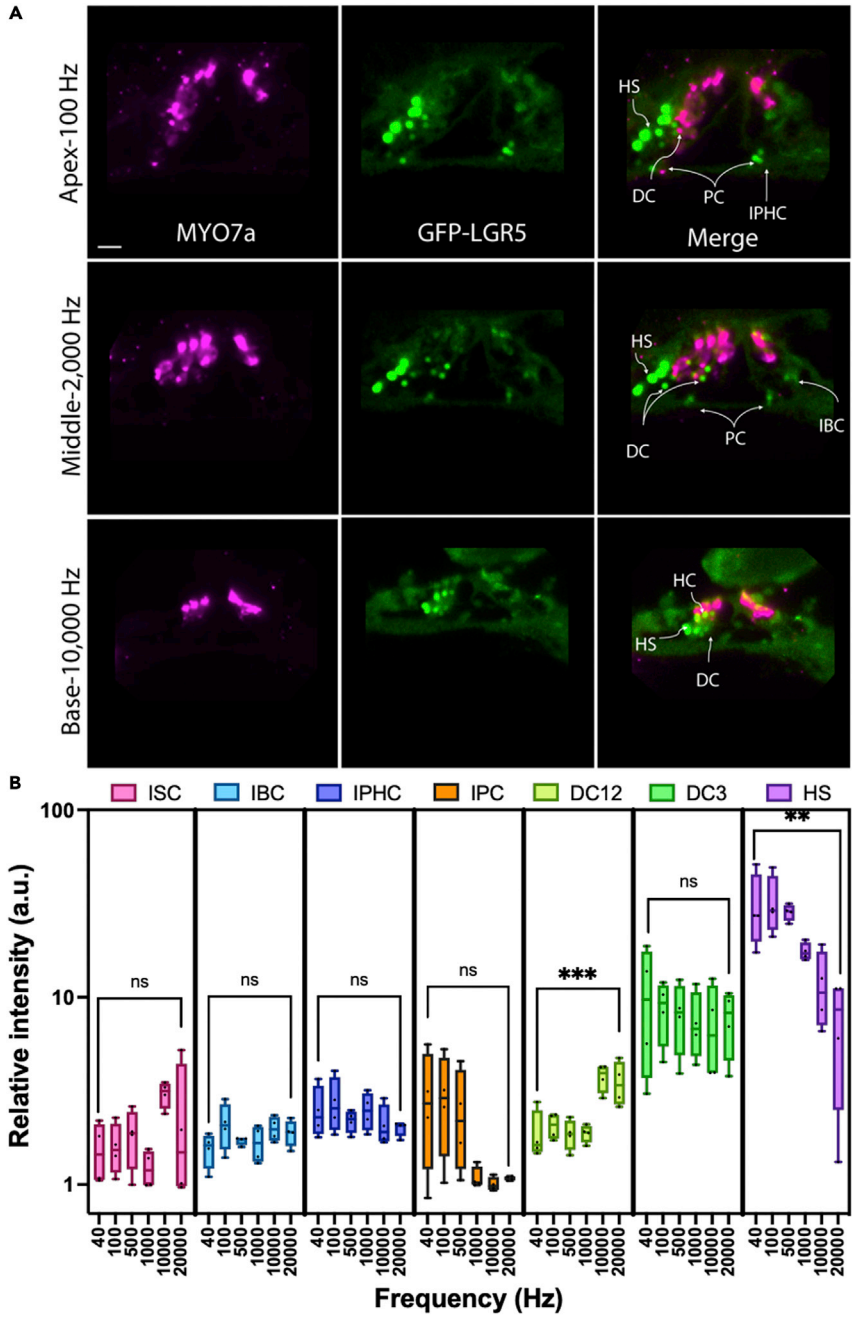

Figure 6. LGR5 expression in supporting cells has a strong dependency on cell location in the organ of Corti

(A) Digital sections of porcine cochlea stained for MYO7a and GFP at P120 (LGR5-H2B-GFP). The supporting cells were assigned to the following groups: GER/ISC, IBC, IPHC, IPC, 1st and 2nd DC (DC12), 3rd DC (DC3), and HS. Scale bar, 20 μm.

(B) The quantification of LGR5 expression at different frequencies and in different supporting cells (number of animals, N = 4; P120). Each point in the graph represents the average relative intensity (LGR5/background) of ten individual cells for each cell type per sample and the standard deviation of all four averaged points in all four samples (mean ± SD) (See Figure S3). The cells' relative intensity expression was measured at the apex (40 Hz and 100 Hz), middle (700 Hz and 2 kHz), and base (10 kHz and 20kHz). The mixed-effect model has been used to find significant differences between the apical and basal LGR5 expression for individual cell types. The stars indicate the level of significance. If a p-value is less than 0.05, it is represented with one star (*), a p-value less than 0.01 is marked with two stars (**), and less than 0.001 with three stars (***). If the p-value is above 0.05, it is shown as ns. Only in the base, the DC12 group might include HCs (See Figures S4–S6 and Table. S1).

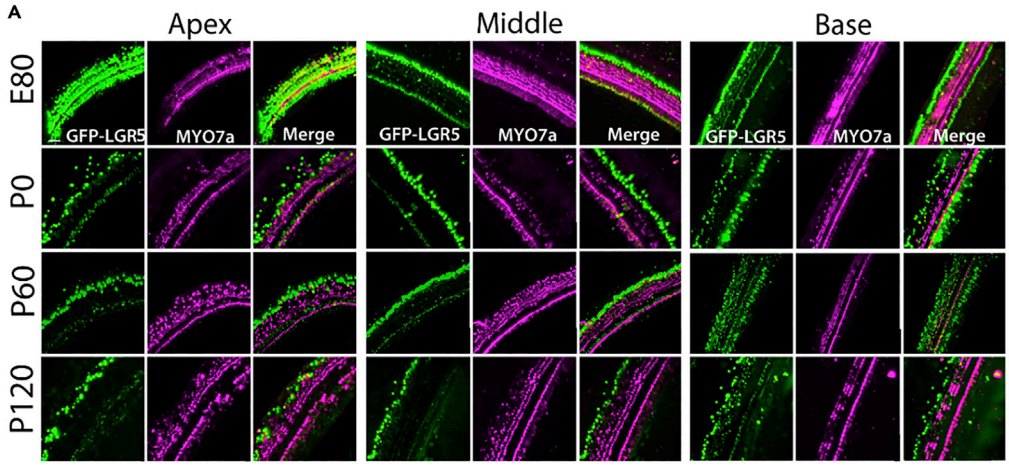

B

Frequency (Hz)	Age	GER	ISC	IBC	IPHC	IPC	DC12	DC3	HS
40	E80								
	P0								
	P60								
	P120								
100	E80								
	P0								
	P60								
	P120								
500	E80								
	P0								
	P60								
	P120								
1000	E80								
	P0								
	P60								
	P120								
10000	E80								
	P0								
	P60								
	P120								
20000	E80								
	P0								
	P60								
	P120								

Figure 7. LGR5 expression in supporting cells changes with age

(A) Digital sections of the porcine cochlea were stained for MYO7a (Hair cells) and GFP (LGR5) at the apex, middle, and base of the cochlea. The images were extracted from LGR5-H2B-GFP transgenic pigs (E80, P0, P60, and P120). Scale bar, 30 μm.

(B) The quantification of LGR5 expression across ages at the apex (40 and 100 Hz), middle (700 and 2000 Hz), and base (10 and 20 kHz) of the cochlea. We have reported the log of the average LGR5 intensity of each cell type across four samples/cochleae at each age and provided the individual frequencies. For this measurement in each cochlea, ten cells from each supporting cell subset were selected and quantified per cochlea (number of cochleae, N = 4 for each age, and a total of 16 cochleae). Please note, that the GER population only exists at the E80 stage (See Figure S6 and Table. S2).

we documented changes in the position of the supporting cells at low frequencies. Establishing a methodology to study large animal cochlea and documenting changes in the low-frequency range set the stage for future hearing studies. For example, recent exciting reports aimed to replace conventional cochlear implants, which rely on electrical stimulation, with optogenetic stimulation of cochlear neurons using a light beam in gerbils (Wrobel et al., 2018). These studies attempt to deliver cell-specific light stimulation based on cell location in the organ of Corti to improve auditory-driven behavior. Consequently, dense LED arrays are implanted into the inner ear to account for the small ear size; the large porcine cochlea will pose fewer restrictions on miniaturization and benefit translational work. The availability of pigs, that are easy to breed, together with new approaches to investigate optical implants in tissues (Kahan et al., 2021), could potentially be significant enablers for such technology development efforts.

We have determined that cochlear development in pigs requires about 10–11 weeks from the time that the cochlear ducts are formed at E38 until E115/P0 where we observed full maturation. This developmental duration is closer to humans (GW10-GW24) (Hosoya et al., 2021; Johnson Chacko et al., 2019), contrasting the 3 weeks duration in mice (E14.5-P14) (Kopecky et al., 2012). Thus, studying cochlear development in the porcine model could be beneficial for the detection of transient gene expression and to examine temporal changes in fetal cochlear development at high resolution. Our results suggest that the porcine model is suitable for precise observations of cochlear development and may lead to new findings that would be missed in a mouse model as the transient genes might exist for a longer time. For example, Na-K-Cl cotransporter 1 (NKCC1) is expressed transiently in the stria vascularis during development for common marmosets, whereas it is not reported in mice (Hosoya et al., 2021). Our results improve our understanding of inner ear development in pigs and provide a basis for time-specific or cell type-specific transgenic models for further regeneration studies.

Multiple rodent models have brought exciting insights into the molecular pathways that lead to normal and impaired hearing, and provide platforms for evaluating therapeutic interventions (e.g., small molecules and genetic perturbations using viral vectors). However, the major differences between rodents and humans have led to two main challenges: (*1*) in some instances, transgenic mice carrying genetic mutations implicated in human hearing loss fail to exhibit the phenotype (e.g., *GRHL2* or *CX31*) (Hosoya et al., 2016). (*2*) The size and anatomy of the rodent's inner ear and its protective barriers do not match those of humans. The size mismatch creates a significant challenge for a detailed evaluation of the human inner ear and future assessment of the translational potential of non-invasive methods to deliver small molecules or viral vectors to the human inner ear. Here, we have shown that pigs have a cochlear size and basilar membrane length similar to humans–unlike rodents, some mammals such as cats, and even non-human primate e.g., marmosets. The similar size provides an opportunity to facilitate the translation of novel approaches for hearing restoration and closer genome could fill the mechanistic gaps where rodent models do not recapitulate the human phenotype.

Additionally, 3D imaging compared to traditional 2D methods provides increased accuracy in cellular morphological measurements such as cellular length. The standard deviation in the measurement performed using 3D images was half of that associated with the measurement done in 2D images. Previous studies that used 2D immunohistology images showed large variability in the measurement specifically for long hair cells at the apex, SD > 8 μm or more (Pujol et al., 1992; Zetes et al., 2012). This large SD in the measurements using 2D images is in accord with our measurement values of the hair cell lengths in 2D images. The 3D method also provides other benefits such as access to all the regions of the cochlea as it retains the whole structure. In previous studies, access to certain cells in specific areas has been reported to fail owing to cells not retaining their original shape after sectioning (guinea pig data from Zetes et al. 2012).

Despite all the benefits provided by tissue clearing and 3D imaging, there are some shortcomings including long processing time, quenching of genetically expressed fluorescence, limitations on useable antibodies, and tissue shrinkage (Molbay et al., 2021). If the shrinkage is not uniform in all axes, the tissue can be deformed, and therefore morphological comparison to previous studies is always advised. Please note that the literature on tissue clearing indicates that the shrinkage should be isotropic, but these conclusions were derived in the soft tissue (mainly brains) (Ertürk et al., 2012). The cochlea is different from soft tissue, as there are many interfaces between hard and soft tissue, and we believe that maximum distortions could occur in these interfaces.

We also acknowledge that every histological method has the potential to distort the native structure. We are relatively confident that the macro-organization of the cells along the organ of Corti has not been distorted by our clearing process. For instance, the line structure of the hair cells is maintained; therefore, we have no reason to believe that the line structure of the supporting cells will be dramatically distorted. Qualitatively, we also compared our results to the literature. A 2D immunohistology of the pig cochlea (Rask-Andersen et al., 2010) revealed cytoarchitecture which is consistent with our 3D tissue clearing results. This confirms that the cell locations are roughly preserved and not dramatically affected by tissue clearing. Using tissue clearing, as the organ of Corti is not extracted and dissected, the cytoarchitecture of the organ of Corti has the potential to be more preserved in comparison with 2D immunohistology methods (Neckel et al., 2016; Molbay et al., 2021).

In addition to morphological studies, we quantified LGR5 expression based on cell location in the organ of Corti and across ages (E80 to P120). Observing changes in LGR5 expression could help unlock the role of the Wnt signaling pathway in development and repair, as well as support alternative therapeutic approaches for hair cell regeneration. The assignment of cell types for the quantification of LGR5 intensity is based on cell location as supporting cell type-specific markers for pigs have not yet been validated. We also recognize the uncertainty in the accuracy of cell assignment if the cytoarchitecture of the organ of Corti is modified during tissue clearing, but there is no evidence that significant changes have occurred. All our measurements were based on the organized row structure of the supporting cells, and the reproducibility of the data from multiple cross-sections supports our conclusions.

Based on this approach overall, the following observations regarding LGR5 expression were noted: (1) LGR5 expression at the apex was mainly in the GER, DC3, and HS, while at the base the LGR5 expression was observed in all three rows of DC, HS, ISC, and hair cells. The lower expression in GER, IBC, and IPHC at the base in comparison to the apex and older ages coincide with increasing cochlear maturation from base to apex (Rubel, 1984). This observation is important as it has been shown that GER, IBC, and IPHC have regenerative capacity and can transdifferentiate into hair cells before the cochlea matures (Chai et al., 2012; Kubota et al., 2021; Mellado Lagarde et al., 2014; Waldhaus et al., 2015). (2) The HS express LGR5 with high intensity (relative log intensity above 1.3) throughout the cochlea at all ages. HS exhibit regenerative capacity but has not been shown to express LGR5 in murine models (White et al., 2006). It will be interesting to explore this observation in humans. (3) In the mature cochlea, we observed LGR5 expression in hair cells, primarily in the basal turn of cochlea (responsible for detecting high-frequency sound). Distinguishing between the LGR5 expression of hair cells from DC12 is not feasible from surface view at the frequency of ~20 kHz as they project onto the same plane. As such, some of the expressions detected in LGR5 expression quantification of DC12 at 20 kHz might be related to hair cells as marked in the base quantification (Figure S6 and Figure 7). The LGR5 expression at the middle frequencies belonged only to DC12 as our radial view images showed that hair cells do not express LGR5 at these frequencies (Figure S5). Although LGR5 expression has been reported in developing hair cells in rodents (Chai et al., 2012), the extent of expression is not comparable to the observation in the porcine model. These observations suggest differences in LGR5 expression between species and might indicate the possibility of different LGR5 patterns in humans. (4) In immature cochleae (E80), the GER, IBC, and IPHC significantly lose LGR5 expression towards the base. While in mature cochleae, ISC and DC12 show a significant increase in LGR5 expression towards the base. This increasing trend has not been reported before for any model to the best of our knowledge and requires further investigation. (5) All cell types except for IPC manifest a significant decrease in LGR5 expression with aging. This result is in line with the literature suggesting that LGR5 expression is elevated during embryogenesis and gradually declines (Chai et al., 2011; Shi et al., 2012). (6) From the comparison between cell types we observed: i) The HS in all frequencies are expressing LGR5 more than other cells. ii) The DC3, after HS, express LGR5 at higher levels than other cell types in the middle and apical turns. iii) The IPHC and IBC have higher LGR5 intensities in comparison to pillar cells in most frequencies. iv) The LGR5 expression level between DC12 and DC3 at the base becomes comparable. Documentation of changes in LGR5 expression across ages and cell location in the organ of Corti highlights the importance of the ability to register and compare cell locations across different cochlea.

We recognized that the H2B-GFP turnover might affect some of the intensity qualifications but we believe the impact of turnover is minimal for three reasons: (1) A previous study shows that GFP protein expression correlates with LGR5 mRNA expression in the skin of the same pig model used in this study (Polkoff et al., 2020, 2022). (2) In the literature, the half-life for H2B-GFP is variable, and it depends on many factors such as cell turnover and activity, ranging from 4 to 8 h for dividing cells (Liu et al., 2021; Xenopoulos et al., 2015) to 4–6 weeks into hematopoietic and epithelial stem cells (Morcos et al., 2020; SanjeevWaghmare et al., 2008). Although supporting cells are shown to proliferate *in vitro* within 1–3 days (White et al., 2006), they are postmitotic *in vivo* (Ruben, 1967). From the literature, we can indicate that most supporting cells do not divide after maturation and the turnover rate is similar for all subsets. In the apex of the DC12 supporting cell subset, the intensity of LGR5 drops from an average of 11.08 at E80 to 0.93 at P0 within 35 days. This means the half-life for DC12 cells is less than 35/2 ~2.5 weeks. Thus, we can estimate that the half-life in this study is somewhere between (2–3 weeks), and therefore, the turnover time is less than the time points in this study, which are mostly at 60-day intervals (8.5 weeks). (3) Last, we found two trends in the LGR5 expression over time that are independent of H2B turnover: i) The increasing trend for LGR5 expression in cell types such as ISC and DC12. ii) Constant LGR5 expression in cells such as in HS across a period of 155 days.

After establishing that the morphology and expression of the LGR5 are changing as a function of frequency, future work could include the quantification of the expression pattern of other important genes and transcriptional factors that are important in hearing research and regeneration (e.g., Fzd9, Sox9, Shh, Sox2, Atoh1) (Atkinson et al., 2018; Kempfle et al., 2016; Lee et al., 2020; Lu et al., 2013; Zhang et al., 2019, 2020). The 3D imaging will facilitate this effort, as it provides an accurate registration procedure for comparisons among specimens. Beyond the porcine model, the availability of a platform that will facilitate frequency-specific tracking of proteins and transcription factors in the cochlea of a large animal model is useful. This platform could provide a basis for evaluating new treatment methods and exploring their impact on selective frequency perception.

Limitations of the study

We recognize some limitations in this study. First, in our LGR5 quantifications, we assigned the cell type of GFP positive cells based on their locations and macro-organization. A more accurate approach would have used cell type-specific markers, but we did not use this approach as cell type-specific markers have not been validated for pigs. Therefore, we recognize that if the cytoarchitecture of the organ of Corti is not well preserved, some ambiguity might exist. To overcome this uncertainty, cell type-specific markers for pigs need to be validated. Second, regardless of the advantages provided by tissue clearing and 3D imaging for studying the cochlea, they inherently have several disadvantages: long tissue processing time per sample, the quenching of endogenous fluorescence, antibody compatibility issues, and last, the requirement for technical expertise to analyze large datasets of images.

STAR★METHODS

Detailed methods are provided in the online version of this paper and include the following:

- KEY RESOURCES TABLE
- RESOURCE AVAILABILITY
  - Lead contact
  - Materials availability
  - Data and code availability
- EXPERIMENTAL MODEL AND SUBJECT DETAILS
  - Animals
  - Institutional permissions
- METHOD DETAILS
  - BoneClear tissue clearing
  - Custom-build light-sheet microscopy
- QUANTIFICATION AND STATISTICAL ANALYSIS
  - Basilar membrane tracing
  - Hair cell length measurement
  - Denoising
  - Hair cell counting
  - Quantification of LGR5 expression
  - Control
  - Exclusion criteria
- STATISTICAL ANALYSIS

SUPPLEMENTAL INFORMATION

Supplemental information can be found online at https://doi.org/10.1016/j.isci.2022.104695.

ACKNOWLEDGMENTS

The authors would like to thank the NCSU Central Procedure Lab for their help with tissue collection. We would like to thank Dr. Patrick J Atkinson for his comments and revision to improve the article. We also would like to thank Laura Edwards for her help with animal tissue collection and Kathryn Polkoff for her help with the animal model.

Funding: Comparative Medicine Institute, Young Scholar Award. Comparative Medicine Institute, Functional Tissue Engineering Cross-disciplinary Research Initiation Funding. National Institute of Health (NIH), NIDCD Ro1DC016919.

AUTHOR CONTRIBUTIONS

Conceptualization: AM, AG, FSL, Methodology: AM, CL, SS, YC, JR, JAP, Investigation: AM, Visualization: AM, Resources: JAP, Supervision: AG, FSL, AGLC, Writing—original draft: AM, Writing—review & editing: AM, AG, FSL, AGLC.

DECLARATION OF INTERESTS

The authors declare no competing interests.

INCLUSION AND DIVERSITY

We worked to ensure sex balance in the selection of non-human subjects. One or more of the authors of this paper self-identifies as an underrepresented ethnic minority in science.

Received: January 19, 2022
Revised: April 20, 2022
Accepted: June 27, 2022
Published: August 19, 2022

REFERENCES

Anderson, N.C., Thomovsky, S.A., Lucas, J.R., Kushiro-Banker, T., Radcliffe, J.S., Stewart, K.R., and Lay, D.C., Jr. (2019). Auditory brainstem responses in weaning pigs and three ages of sows1. Transl. Animal Sci. *3*, 1416–1422. https://doi.org/10.1093/tas/txz123.

Ashmore, J. (2008). Cochlear outer hair cell motility. Physiol. Rev. *88*, 173–210. https://doi.org/10.1152/physrev.00044.2006.

Atkinson, P.J., Dong, Y., Gu, S., Liu, W., Najarro, E.H., Udagawa, T., and Cheng, A.G. (2018). Sox2 haploinsufficiency primes regeneration and Wnt responsiveness in the mouse cochlea. J. Clin. Invest. *128*, 1641–1656. https://doi.org/10.1172/JCI97248.

Barker, N., Rookmaaker, M., Kujala, P., Ng, A., Leushacke, M., Snippert, H., van de Wetering, M., Tan, S., Van Es, J., Huch, M., et al. (2012). Lgr5+ve stem/progenitor cells contribute to nephron formation during kidney development. Cell Rep. *2*, 540–552. https://doi.org/10.1016/j.celrep.2012.08.018.

Basch, M.L., Brown, R.M., II, Jen, H.-I., and Groves, A.K. (2016). Where hearing starts: the development of the mammalian cochlea. J. Anat. *228*, 233–254. https://doi.org/10.1111/joa.12314.

Berg, S., Kutra, D., Kroeger, T., Straehle, C.N., Kausler, B.X., Haubold, C., Schiegg, M., Ales, J., Beier, T., Rudy, M., et al. (2019). ilastik: interactive machine learning for (bio)image analysis. Nat. Methods *16*, 1226–1232. https://doi.org/10.1038/s41592-019-0582-9.

Bramhall, N.F., Shi, F., Arnold, K., Hochedlinger, K., and Edge, A. (2014). Lgr5-Positive supporting cells generate new hair cells in the postnatal cochlea. Stem Cell Rep. *2*, 311–322. https://doi.org/10.1016/j.stemcr.2014.01.008.

Bria, A., and Iannello, G. (2012). TeraStitcher - a tool for fast automatic 3D-stitching of teravoxel-sized microscopy images. BMC Bioinf. *13*, 316. https://doi.org/10.1186/1471-2105-13-316.

Burns, E.M., Arehart, K.H., and Campbell, S.L. (1992). Prevalence of spontaneous otoacoustic emissions in neonates. J. Acoust. Soc. Am. *91*, 1571–1575. https://doi.org/10.1121/1.402438.

Chai, R., Kuo, B., Wang, T., Liaw, E.J., Xia, A., Jan, T.A., Liu, Z., Taketo, M.M., Oghalai, J.S., Nusse, R., et al. (2012). Wnt signaling induces proliferation of sensory precursors in the postnatal mouse cochlea. Proc. Natl. Acad. Sci. USA *109*, 8167–8172. https://doi.org/10.1073/pnas.1202774109.

Chai, R., Xia, A., Wang, T., Jan, T.A., Hayashi, T., Bermingham-McDonogh, O., and Cheng, A.G.-L. (2011). Dynamic expression of Lgr5, a Wnt target gene, in the developing and mature mouse cochlea. J. Assoc. Res. Otolaryngol. *12*, 455–469. https://doi.org/10.1007/s10162-011-0267-2.

West, C.D. (1985). The relationship of the spiral turns of the cochlea and the length of the basilar membrane to the range of audible frequencies in ground dwelling mammals. J. Acoust. Soc. Am. *77*, 1091–1101. https://doi.org/10.1121/1.392227.

Cox, B.C., Chai, R., Lenoir, A., Liu, Z., Zhang, L., Nguyen, D.-H., Chalasani, K., Steigelman, K.A., Fang, J., Cheng, A.G., and Zuo, J. (2014). Spontaneous hair cell regeneration in the neonatal mouse cochlea in vivo. Development *141*, 816–829. https://doi.org/10.1242/dev.103036.

Dai, Y., Vaught, T.D., Boone, J., Chen, S.-H., Phelps, C.J., Ball, S., Monahan, J.A., Jobst, P.M., McCreath, K.J., Lamborn, A.E., et al. (2002). Targeted disruption of the α1, 3-galactosyltransferase gene in cloned pigs. Nat. Biotechnol. *20*, 251–255. https://doi.org/10.1038/nbt0302-251.

Engel, J. (2008). Gerbils can tune in. J. Physiol. *586*, 919. https://doi.org/10.1113/jphysiol.2007.150409.

Engström, H., Ades, H.W., and Hawkins, J.E. (1964). Cytoarchitecture of the organ of Corti. Acta Otolaryngol. *57*, 92–99. https://doi.org/10.3109/00016486409134545.

Ertürk, A., Becker, K., Jährling, N., Mauch, C.P., Hojer, C.D., Egen, J.G., Hellal, F., Bradke, F., Sheng, M., and Dodt, H.-U. (2012). Three-dimensional imaging of solvent-cleared organs using 3DISCO. Nat. Protoc. *7*, 1983–1995. https://doi.org/10.1038/nprot.2012.119.

Farooq, R., Hussain, K., Tariq, M., Farooq, A., and Mustafa, M. (2020). CRISPR/Cas9: targeted genome editing for the treatment of hereditary hearing loss. J. Appl. Genet. *61*, 51–65. https://doi.org/10.1007/s13353-019-00535-6.

Fay, R.R. (2012). Comparative Hearing: Mammals (Springer).

Békésy, G., Wever, E.G., and Peake, W.T. (1990). Experiments in hearing. J. Acoust. Soc. Am. *88*, 2905. https://doi.org/10.1121/1.399656.

Greenbaum, A., Chan, K.Y., Dobreva, T., Brown, D., Balani, D.H., Boyce, R., Kronenberg, H.M., McBride, H.J., and Gradinaru, V. (2017). Bone CLARITY: clearing, imaging, and computational analysis of osteoprogenitors within intact bone marrow. Sci. Transl. Med. *9*, eaah6518. https://doi.org/10.1126/scitranslmed.aah6518.

Greenwood, D.D. (1990). A cochlear frequency-position function for several species–29 years later. J. Acoust. Soc. Am. *87*, 2592–2605. https://doi.org/10.1121/1.399052.

Guo, W., and Yang, S.m. (2015). Advantages of a miniature pig model in research on human hereditary hearing loss. J. Otolaryngol. *10*,

105–107. https://doi.org/10.1016/j.joto.2015.11.001.

Guo, W., Yi, H., Ren, L., Chen, L., Zhao, L., Sun, W., and Yang, S.-M. (2015). The morphology and electrophysiology of the cochlea of the miniature pig. Anat. Rec. *298*, 494–500. https://doi.org/10.1002/ar.23095.

Gurr, A., Kevenhörster, K., Stark, T., Pearson, M., and Dazert, S. (2009). The common pig: a possible model for teaching ear surgery. Eur. Arch. Oto-Rhino-Laryngol. *267*, 213–217. https://doi.org/10.1007/s00405-009-1040-6.

Spoendlin, H., Plomp, R., and Guido, F.S. (1970). Frequency Analysis and Periodicity Detection in Hearing: [The Proceedings of the International Symposium on Frequency Analysis and Periodicity, the Netherlands, June 23-27, 1969] (Sijthoff).

Haegebarth, A., and Clevers, H. (2009). Wnt signaling, Lgr5, and stem cells in the intestine and skin. Am. J. Pathol. *174*, 715–721. https://doi.org/10.2353/ajpath.2009.080758.

Hai, T., Guo, W., Yao, J., Cao, C., Luo, A., Qi, M., Wang, X., Wang, X., Huang, J., Zhang, Y., et al. (2017). Creation of miniature pig model of human Waardenburg syndrome type 2A by ENU mutagenesis. Hum. Genet. *136*, 1463–1475. https://doi.org/10.1007/s00439-017-1851-2.

Heffner, H., and Masterton, B. (1980). Hearing in Glires: domestic rabbit, cotton rat, feral house mouse, and kangaroo rat. J. Acoust. Soc. Am. *68*, 1584–1599. https://doi.org/10.1121/1.385213.

Heffner, H.E., and Heffner, R.S. (2007). Hearing ranges of laboratory animals. J. Am. Assoc. Lab. Anim. Sci. *46*, 20–22.

Heffner, R., Heffner, H., and Masterton, B. (1971). Behavioral measurements of absolute and frequency-difference thresholds in Guinea pig. J. Acoust. Soc. Am. *49*, 1888–1895. https://doi.org/10.1121/1.1912596.

Heffner, R.S., and Heffner, H.E. (1985). Hearing range of the domestic cat. Hear. Res. *19*, 85–88. https://doi.org/10.1016/0378-5955(85)90100-5.

Heffner, R.S., and Heffner, H.E. (1990). Hearing in domestic pigs (Sus scrofa) and goats (Capra hircus). Hear. Res. *48*, 231–240. https://doi.org/10.1016/0378-5955(90)90063-u.

Heffner, R.S., and Heffner, H.E. (1991). Behavioral hearing range of the chinchilla. Hear. Res. *52*, 13–16. https://doi.org/10.1016/0378-5955(91)90183-A.

Hornsby, B.W.Y., and Ricketts, T.A. (2006). The effects of hearing loss on the contribution of high- and low-frequency speech information to speech understanding. II. Sloping hearing loss. J. Acoust. Soc. Am. *119*, 1752–1763. https://doi.org/10.1121/1.2161432.

Hosoya, M., Fujioka, M., Murayama, A.Y., Okano, H., and Ogawa, K. (2021). The common marmoset as suitable nonhuman alternative for the analysis of primate cochlear development. FEBS J. *288*, 325–353. https://doi.org/10.1111/febs.15341.

Hosoya, M., Fujioka, M., Ogawa, K., and Okano, H. (2016). Distinct expression patterns of causative genes responsible for hereditary progressive hearing loss in non-human primate cochlea. Sci. Rep. *6*, 22250. https://doi.org/10.1038/srep22250.

Hutson, K.A., Pulver, S.H., Ariel, P., Naso, C., and Fitzpatrick, D.C. (2021). Light sheet microscopy of the gerbil cochlea. J. Comp. Neurol. *529*, 757–785. https://doi.org/10.1002/cne.24977.

Igarashi, Y., and Ishii, T. (1980). Embryonic development of the human organ of Corti: electron microscopic study. Int. J. Pediatr. Otorhinolaryngol. *2*, 51–62. https://doi.org/10.1016/0165-5876(80)90028-2.

Johnson Chacko, L., Wertjanz, D., Sergi, C., Dudas, J., Fischer, N., Eberharter, T., Hoermann, R., Glueckert, R., Fritsch, H., Rask-Andersen, H., et al. (2019). Growth and cellular patterning during fetal human inner ear development studied by a correlative imaging approach. BMC Dev. Biol. *19*, 11. https://doi.org/10.1186/s12861-019-0191-y.

Johnson, L.A., Santina, C.C.D., and Wang, X. (2012). Temporal bone characterization and cochlear implant feasibility in the common marmoset (Callithrix jacchus). Hear. Res. *290*, 37–44. https://doi.org/10.1016/j.heares.2012.05.002.

Kahan, A., Greenbaum, A., Jang, M.J., Robinson, J.E., Cho, J.R., Chen, X., Kassraian, P., Wagenaar, D.A., and Gradinaru, V. (2021). Light-guided sectioning for precise in situ localization and tissue interface analysis for brain-implanted optical fibers and GRIN lenses. Cell Rep. *36*, 109744. https://doi.org/10.1016/j.celrep.2021.109744.

Kempfle, J.S., Turban, J.L., and Edge, A.S.B. (2016). Sox2 in the differentiation of cochlear progenitor cells. Sci. Rep. *6*, 23293. https://doi.org/10.1038/srep23293.

Keppeler, D., Kampshoff, C.A., Thirumalai, A., Duque-Afonso, C.J., Schaeper, J.J., Quilitz, T., Töpperwien, M., Vogl, C., Hessler, R., Meyer, A., et al. (2021). Multiscale photonic imaging of the native and implanted cochlea. Proc. Natl. Acad. Sci. USA *118*, e2014472118. https://doi.org/10.1073/pnas.2014472118.

Kim, J., and Koo, M. (2015). Mass and stiffness impact on the middle ear and the cochlear partition. J Audiol Otol *19*, 1–6. https://doi.org/10.7874/jao.2015.19.1.1.

Kim, J.H., Rodríguez-Vázquez, J.F., Verdugo-López, S., Cho, K.H., Murakami, G., and Cho, B.H. (2011). Early fetal development of the human cochlea. Anat. Rec. *294*, 996–1002. https://doi.org/10.1002/ar.21387.

Kinzel, B., Pikiolek, M., Orsini, V., Sprunger, J., Isken, A., Zietzling, S., Desplanches, M., Dubost, V., Breustedt, D., Valdez, R., et al. (2014). Functional roles of Lgr4 and Lgr5 in embryonic gut, kidney and skin development in mice. Dev. Biol. *390*, 181–190. https://doi.org/10.1016/j.ydbio.2014.03.009.

Knoll, R.M., Reinshagen, K.L., Barber, S.R., Ghanad, I., Swanson, R., Smith, D.H., Abdullah, K.G., Jung, D.H., Remenschneider, A.K., and Kozin, E.D. (2019). High resolution computed tomography atlas of the porcine temporal bone and skull base: anatomical correlates for traumatic brain injury research. J. Neurotrauma *36*, 1029–1039. https://doi.org/10.1089/neu.2018.5808.

Kopecky, B., Johnson, S., Schmitz, H., Santi, P., and Fritzsch, B. (2012). Scanning thin-sheet laser imaging microscopy elucidates details on mouse ear development. Dev. Dynam. *241*, 465–480. https://doi.org/10.1002/dvdy.23736.

Kristensen, S., and Gimsing, S. (1988). Brief communication: occupational hearing impairment in pig breeders. Scand. Audiol. *17*, 191–192. https://doi.org/10.3109/01050398809042192.

Kubota, M., Scheibinger, M., Jan, T.A., and Heller, S. (2021). Greater epithelial ridge cells are the principal organoid-forming progenitors of the mouse cochlea. Cell Rep. *34*, 108646. https://doi.org/10.1016/j.celrep.2020.108646.

Lee, S., Song, J.-J., Beyer, L.A., Swiderski, D.L., Prieskorn, D.M., Acar, M., Jen, H.-I., Groves, A.K., and Raphael, Y. (2020). Combinatorial Atoh1 and Gfi1 induction enhances hair cell regeneration in the adult cochlea. Sci. Rep. *10*, 21397. https://doi.org/10.1038/s41598-020-78167-8.

Lenz, D.R., Gunewardene, N., Abdul-Aziz, D.E., Wang, Q., Gibson, T.M., and Edge, A.S.B. (2019). Applications of Lgr5-positive cochlear progenitors (LCPs) to the study of hair cell differentiation. Front. Cell Dev. Biol. *7*, 14. https://doi.org/10.3389/fcell.2019.00014.

Li, C., Li, C., Zhang, X., Troy Ghashghaei, H., Greenbaum, A., Zhang, X., Ghashghaei, H.T., Ghashghaei, H.T., Greenabum, A., Greenabum, A., et al. (2021a). Deep learning-based autofocus method enhances image quality in light-sheet fluorescence microscopy. Biomed. Opt. Express *12*, 5214. https://doi.org/10.1364/BOE.427099.

Li, H., Helpard, L., Ekeroot, J., Rohani, S.A., Zhu, N., Rask-Andersen, H., Ladak, H.M., and Agrawal, S. (2021b). Three-dimensional tonotopic mapping of the human cochlea based on synchrotron radiation phase-contrast imaging. Sci. Rep. *11*, 4437. https://doi.org/10.1038/s41598-021-83225-w.

Liu, Y., Wang, Y., Yang, L., Sun, F., Li, S., Wang, Y., Zhang, G.-A., Dong, T., Zhang, L.-L., Duan, W., et al. (2021). The nucleolus functions as the compartment for histone H2B protein degradation. iScience *24*, 102256. https://doi.org/10.1016/j.isci.2021.102256.

Locher, H., Frijns, J.H., van Iperen, L., de Groot, J.C., Huisman, M.A., and Chuva de Sousa Lopes, S.M. (2013). Neurosensory development and cell fate determination in the human cochlea. Neural Dev. *8*, 20. https://doi.org/10.1186/1749-8104-8-20.

Lovell, J.M., and Harper, G.M. (2007). The morphology of the inner ear from the domestic pig (Sus scrofa). J. Microsc. *228*, 345–357. https://doi.org/10.1111/j.1365-2818.2007.01852.x.

Lu, N., Chen, Y., Wang, Z., Chen, G., Lin, Q., Chen, Z.-Y., and Li, H. (2013). Sonic hedgehog initiates cochlear hair cell regeneration through downregulation of retinoblastoma protein. Biochem. Biophys. Res. Commun. *430*, 700–705. https://doi.org/10.1016/j.bbrc.2012.11.088.

Lunney, J.K. (2007). Advances in swine biomedical model genomics. Int. J. Biol. Sci. *3*, 179–184. https://doi.org/10.7150/ijbs.3.179.

Luong, Q.V., Israel, A., Sharma, R., Ussar, S., and Lee, K.Y. (2021). Development of an optimized clearing protocol to examine adipocyte subpopulations in white adipose tissue. Methods Protocols *4*, 39. https://doi.org/10.3390/mps4020039.

Manoussaki, D., Chadwick, R.S., Ketten, D.R., Arruda, J., Dimitriadis, E.K., and O'Malley, J.T. (2008). The influence of cochlear shape on low-frequency hearing. Proc. Natl. Acad. Sci. USA *105*, 6162–6166. https://doi.org/10.1073/pnas.0710037105.

McLean, W.J., Yin, X., Lu, L., Lenz, D.R., McLean, D., Langer, R., Karp, J.M., and Edge, A.S. (2017). Clonal expansion of Lgr5-positive cells from mammalian cochlea and high-purity generation of sensory hair cells. Cell Rep. *18*, 1917–1929. https://doi.org/10.1016/j.celrep.2017.01.066.

Mellado Lagarde, M.M., Wan, G., Zhang, L., Gigliello, A.R., McInnis, J.J., Zhang, Y., Bergles, D., Zuo, J., and Corfas, G. (2014). Spontaneous regeneration of cochlear supporting cells after neonatal ablation ensures hearing in the adult mouse. Proc. Natl. Acad. Sci. USA *111*, 16919–16924. https://doi.org/10.1073/pnas.1408064111.

Moatti, A., Cai, Y., Li, C., Sattler, T., Edwards, L., Piedrahita, J., Ligler, F.S., and Greenbaum, A. (2020). Three-dimensional imaging of intact porcine cochlea using tissue clearing and custom-built light-sheet microscopy. Biomed. Opt. Express *11*, 6181. https://doi.org/10.1364/BOE.402991.

Montgomery, S.C., and Cox, B.C. (2016). Whole mount dissection and immunofluorescence of the adult mouse cochlea. JoVE *53561*. https://doi.org/10.3791/53561.

Morcos, M.N.F., Zerjatke, T., Glauche, I., Munz, C.M., Ge, Y., Petzold, A., Reinhardt, S., Dahl, A., Anstee, N.S., Bogeska, R., et al. (2020). Continuous mitotic activity of primitive hematopoietic stem cells in adult mice. J. Exp. Med. *217*, e20191284. https://doi.org/10.1084/jem.20191284.

Molbay, M., Kolabas, Z.I., Todorov, M.I., Ohn, T.-L., and Ertürk, A. (2021). A guidebook for DISCO tissue clearing. Mol. Syst. Biol. *17*, e9807. https://doi.org/10.15252/msb.20209807.

Neckel, P.H., Mattheus, U., Hirt, B., Just, L., and Mack, A.F. (2016). Large-scale tissue clearing (PACT): technical evaluation and new perspectives in immunofluorescence, histology and ultrastructure. Sci. Rep. *6*, 34331. https://doi.org/10.1038/srep34331.

Polkoff, K.M., Chung, J., Simpson, S.G., Gleason, K., and Piedrahita, J.A. (2020). In vitro validation of transgene expression in gene-edited pigs using CRISPR transcriptional activators. CRISPR J. *3*, 409–418. https://doi.org/10.1089/crispr.2020.0037.

Polkoff, K.M., Gupta, N.K., Green, A.J., Murphy, Y., Chung, J., Gleason, K.L., Simpson, S.G., Walker, D.M., Collins, B., and Piedrahita, J.A. (2022). LGR5 is a conserved marker of hair follicle stem cells in multiple species and is present early and throughout follicle morphogenesis. Sci. Rep. *12*, 9104. https://doi.org/10.1038/s41598-022-13056-w.

Pujol, R., Lenoir, M., Ladrech, S., Tribillac, F., and Rebillard, G. (1992). Correlation between the length of outer hair cells and the frequency coding of the cochlea. In Auditory Physiology and Perception, Y. Cazals, K. Horner, and L. Demany, eds. (Pergamon)), pp. 45–52.

Purves, D., Augustine, G.J., Fitzpatrick, D., Katz, L.C., LaMantia, A.-S., McNamara, J.O., and Williams, S.M. (2001). The Audible spectrum. In Neuroscience, Second edition (Sinauer Associates).

Rai, M., Li, C., and Greenbaum, A. (2022). Quantitative analysis of illumination and detection corrections in adaptive light sheet fluorescence microscopy. Biomed. Opt. Express *13*, 2960–2974. https://doi.org/10.1364/BOE.454561.

Cantos, R., Cole, L.K., Acampora, D., Simeone, A., and Wu, D.K. (2000). Patterning of the mammalian cochlea. Proc. Natl. Acad. Sci. USA *97*, 11707–11713. https://doi.org/10.1073/pnas.97.22.11707.

Rask-Andersen, H., Liu, W., Boström, M., Pfaller, K., Kinnefors, A., Glueckert, R., and Schrott-Fischer, A. (2010). Immunolocalization of prestin in the human cochlea. Audiol. Med. *8*, 56–62. https://doi.org/10.3109/16513860903320300.

Ring, A., Kim, Y.-M., and Kahn, M. (2014). Wnt/catenin signaling in adult stem cell physiology and disease. Stem Cell Rev. *10*, 512–525. https://doi.org/10.1007/s12015-014-9515-2.

Ruben, R.J. (1967). Development of the inner ear of the mouse: a radioautographic study of terminal mitoses. Acta Otolaryngol. *1967*, 1–44.

Roccio, M., and Edge, A. (2019). Inner ear organoids: new tools to understand neurosensory cell development, degeneration and regeneration. Development. https://doi.org/10.1242/dev.177188.

Roth, B., and Bruns, V. (1992). Postnatal development of the rat organ of Corti. Anat. Embryol. *185*, 571–581. https://doi.org/10.1007/BF00185616.

Rubel, E.W. (1984). Ontogeny of auditory system function. Annu. Rev. Physiol. *46*, 213–229. https://doi.org/10.1146/annurev.ph.46.030184.001241.

Ryan, A. (1976a). Hearing sensitivity of the Mongolian gerbil, Meriones unguiculatis. J. Acoust. Soc. Am. *59*, 1222. https://doi.org/10.1121/1.380961.

Ryan, A. (1976b). Noise-induced threshold shifts in the Mongolian gerbil. J. Acoust. Soc. Am. *60*, S87. https://doi.org/10.1121/1.2003577.

Waghmare, S.K., Bansal, R., Lee, J., Zhang, Y.V., McDermitt, D.J., and Tumbar, T. (2008). Quantitative proliferation dynamics and random chromosome segregation of hair follicle stem cells. EMBO J. *27*, 1309–1320. https://doi.org/10.1038/emboj.2008.72.

Santi, P.A., Johnson, S.B., Hillenbrand, M., Grandpre, P.Z., Glass, T.J., and Leger, J.R. (2009). Thin-sheet laser imaging microscopy for optical sectioning of thick tissues. Biotechniques *46*, 287–294. https://doi.org/10.2144/000113087.

Seishima, R., Leung, C., Yada, S., Murad, K.B.A., Tan, L.T., Hajamohideen, A., Tan, S.H., Itoh, H., Murakami, K., Ishida, Y., et al. (2019). Neonatal Wnt-dependent Lgr5 positive stem cells are essential for uterine gland development. Nat. Commun. *10*, 5378. https://doi.org/10.1038/s41467-019-13363-3.

Shi, F., Kempfle, J.S., and Edge, A.S.B. (2012). Wnt-responsive Lgr5-expressing stem cells are hair cell progenitors in the cochlea. J. Neurosci. *32*, 9639–9648. https://doi.org/10.1523/JNEUROSCI.1064-12.2012.

Tan, S.H., Swathi, Y., Tan, S., Goh, J., Seishima, R., Murakami, K., Oshima, M., Tsuji, T., Phuah, P., Tan, L.T., et al. (2020). AQP5 enriches for stem cells and cancer origins in the distal stomach. Nature *578*, 437–443. https://doi.org/10.1038/s41586-020-1973-x.

Taylor, R.R., Jagger, D.J., and Forge, A. (2012). Defining the cellular environment in the organ of Corti following extensive hair cell loss: a basis for future sensory cell replacement in the cochlea. PLoS One *7*, e30577. https://doi.org/10.1371/journal.pone.0030577.

Trevino, M., Lobarinas, E., Maulden, A.C., and Heinz, M.G. (2019). The chinchilla animal model for hearing science and noise-induced hearing loss. J. Acoust. Soc. Am. *146*, 3710–3732. https://doi.org/10.1121/1.5132950.

Fernandez Vallone, V., Leprovots, M., Ribatallada-Soriano, D., Gerbier, R., Lefort, A., Libert, F., Vassart, G., and Garcia, M.-I. (2020). LGR5 controls extracellular matrix production by stem cells in the developing intestine. EMBO Rep. *21*, e49224. https://doi.org/10.15252/embr.201949224.

Waldhaus, J., Durruthy-Durruthy, R., and Heller, S. (2015). Quantitative high-resolution cellular map of the organ of Corti. Cell Rep. *11*, 1385–1399. https://doi.org/10.1016/j.celrep.2015.04.062.

Wang, Q., Liu, K., Yang, L., Wang, H., and Yang, J. (2019). BoneClear: whole-tissue immunolabeling of the intact mouse bones for 3D imaging of neural anatomy and pathology. Cell Res. *29*, 870–872. https://doi.org/10.1038/s41422-019-0217-9.

Wang, T., Chai, R., Kim, G.S., Pham, N., Jansson, L., Nguyen, D.-H., Kuo, B., May, L.A., Zuo, J., Cunningham, L.L., and Cheng, A.G. (2015). Lgr5+ cells regenerate hair cells via proliferation and direct transdifferentiation in damaged neonatal mouse utricle. Nat. Commun. *6*, 6613. https://doi.org/10.1038/ncomms7613.

White, P.M., Doetzlhofer, A., Lee, Y.S., Groves, A.K., and Segil, N. (2006). Mammalian cochlear supporting cells can divide and trans-differentiate into hair cells. Nature *441*, 984–987. https://doi.org/10.1038/nature04849.

Wrobel, C., Dieter, A., Huet, A., Keppeler, D., Duque-Afonso, C.J., Vogl, C., Hoch, G., Jeschke, M., and Moser, T. (2018). Optogenetic stimulation of cochlear neurons activates the auditory pathway and restores auditory-driven

behavior in deaf adult gerbils. Sci. Transl. Med. *10*, eaao0540. https://doi.org/10.1126/scitranslmed.aao0540.

Xenopoulos, P., Kang, M., Puliafito, A., Di Talia, S., and Hadjantonakis, A.-K. (2015). Heterogeneities in nanog expression drive stable commitment to pluripotency in the mouse blastocyst. Cell Rep. *10*, 1508–1520. https://doi.org/10.1016/j.celrep.2015.02.010.

Xu, C., Ren, W., Zhang, Y., Zheng, F., Zhao, H., Shang, H., Guo, W., and Yang, S. (2020). KIT gene mutation causes deafness and hypopigmentation in Bama miniature pigs. Am. J. Transl. Res. *12*, 5095–5107.

Zetes, D.E., Tolomeo, J.A., and Holley, M.C. (2012). Structure and mechanics of supporting cells in the Guinea pig organ of Corti. PLoS One *7*, e49338. https://doi.org/10.1371/journal.pone.0049338.

Zhang, S., Liu, D., Dong, Y., Zhang, Z., Zhang, Y., Zhou, H., Guo, L., Qi, J., Qiang, R., Tang, M., et al. (2019). Frizzled-9+ supporting cells are progenitors for the generation of hair cells in the postnatal mouse cochlea. Front. Mol. Neurosci. *12*, 184. https://doi.org/10.3389/fnmol.2019.00184.

Zhang, Y., Zhang, S., Zhang, Z., Dong, Y., Ma, X., Qiang, R., Chen, Y., Gao, X., Zhao, C., Chen, F., He, S., and Chai, R. (2020). Knockdown of Foxg1 in Sox9+ supporting cells increases the trans-differentiation of supporting cells into hair cells in the neonatal mouse utricle. Aging *12*, 19834–19851. https://doi.org/10.18632/aging.104009.

Zhao, J., Lai, L., Ji, W., and Zhou, Q. (2019). Genome editing in large animals: current status and future prospects. Natl. Sci. Rev. *6*, 402–420. https://doi.org/10.1093/nsr/nwz013.

Zou, B., Mittal, R., Grati, M., Lu, Z., Shu, Y., Tao, Y., Feng, Y., Xie, D., Kong, W., Yang, S., et al. (2015). The application of genome editing in studying hearing loss. Hear. Res. *327*, 102–108. https://doi.org/10.1016/j.heares.2015.04.016.

STAR★METHODS

KEY RESOURCES TABLE

REAGENT or RESOURCE	SOURCE	IDENTIFIER
Antibodies		
Rabbit anti-MYO7a	Abcam	Ab-3481
Chicken anti-GFP	Aveslabs	GFP-1020
Rabbit anti-PGP9.5 Polyclonal	Proteintech	14730-1-AP
Rabbit anti-SOX2	Abcam	ab97959
Cy™3 AffiniPure Donkey Anti-Rabbit IgG (H + L)	Jackson Laboratory	711-165-152, RRID: AB_2307443
Alexa Fluor® 647 AffiniPure Donkey Anti-Chicken IgY (IgG) (H + L)	Jackson Laboratory	703-605-155, RRID: AB_2340379
Chemicals, peptides, and recombinant proteins		
PBS Powder	Sigma Aldrich	P3813
Triton X-100	Sigma Aldrich	93443
Tween-20	Sigma Aldrich	P9416
DMSO	Sigma Aldrich	D128-1
Donkey Serum	Sigma Aldrich	D9663
Heparin	Sigma Aldrich	H3393
Methanol	Fisher Scientific	A412SK-4
Hydrogen Peroxide 30%	Sigma Aldrich	216763
DiBenzylEther	Sigma Aldrich	108014
32% Paraformaldehyde (formaldehyde), PFA aqueous solution	Electron microscopy sciences	RT 15714-S
EDTA	Sigma Aldrich	EDS
Sucrose	Sigma Aldrich	S0389
NaOH	Sigma Aldrich	S8045
Deoxycholate	Sigma Aldrich	D6750
EDTA-Na	Sigma Aldrich	E5134
Dichloromethane	Sigma Aldrich	270997
Deposited data		
Quantified raw data of LGR5 expression	Mendeley Data	http://doi.org/10.17632/vdw3757cxv.3
Experimental models: Organisms/strains		
LGR5-H2B-GFP Transgenic Pigs	Polkoff et al.,2020	http://doi.org/10.1089/crispr.2020.0037
Yorkshire Pigs	NCSU educational unit farm	N/A
Software and algorithms		
IMARIS	Oxford Instruments	https://imaris.oxinst.com/packages
Ilastik	Berg et al.,2019	https://pubmed.ncbi.nlm.nih.gov/31570887/
Terastitcher	Bria and Iannello, 2012.	https://bmcbioinformatics.biomedcentral.com/articles/10.1186/1471-2105-13–316
ImageJ	Github	https://github.com/imagej
Prism 9.2 graphpad	Graphpad	https://www.graphpad.com/scientific-software/prism/
Biorender	Web application	https://biorender.com/
Other		
TO-PRO™-3 Iodide (642/661)	ThemoFisher	T3605

RESOURCE AVAILABILITY

Lead contact

Further information and requests for resources and reagents should be directed to and will be fulfilled by the lead contact, Adele Moatti (amoatti@ncsu.edu).

Materials availability

This study did not generate new unique reagents.

Data and code availability

The software that were used in this study are listed in the key resources table.

The raw LGR5 intensity measurements have been deposited at Mendeley and are publicly available as of the date of publication. The DOI is listed in the key resources table.

Any additional information required to reanalyze the data reported in this study is available from the lead contact upon reasonable request.

EXPERIMENTAL MODEL AND SUBJECT DETAILS

Animals

Cochleae were extracted from transgenic (LGR5-H2B-GFP) (Polkoff et al., 2020) and wild-type Yorkshire pigs, including eighteen fetuses (Day 38, Day 53, and Day 80 mixed genders), eighteen newborns (P0, mixed gender), six 8–10 weeks old pigs (P60-mixed gender), and twelve 16–18 weeks old (P120-mixed gender).

The 60-day interval between ages is at least twice the half-life of H2B-GFP and prevents an impact on the data from residual GFP expression.

	E38	E53	E80	P0	P60	P120
Yorkshire pigs	2	2	2	13	2	2
Transgenic LGR5-H2B-GFP pigs	2	2	8	5	4	10

Institutional permissions

All animal protocols were approved by the Institutional Animal Care and Use Committee (IACUC) at North Carolina State University, following the standards of the National Institute of Health and Committee on Care and Use of Laboratory Animals.

METHOD DETAILS

BoneClear tissue clearing

The BoneClear (Wang et al., 2019) procedure was optimized for the porcine cochlea; given the size and complexity of pig tissues, systemic perfusion of phosphate-buffered saline (PBS) and paraformaldehyde (PFA) was not conducted. The specimen was typically obtained shortly after euthanasia (~30 min).

1. For ease of cochlea extraction, the first step is to separate the head from the body and cut a rectangular window on top of the skull. The bone striker was used to cut through the dense bone and razor blades were used to cut through the skin and ligaments. Using a spatula, the brain was removed to observe the location of the inner ear. Then, the skull was cut in half, and excess bone around each cochlea was removed using the bone striker. Overall, the cochlea extraction can take ~20 min for a juvenile pig, and ~10 min for a newborn pig (Moatti et al., 2020).
2. Then, the tissues were post-fixed in PBS/0.5% PFA/10% sucrose at room temperature for 2 h. The tissues were further fixed in PBS/0.5% PFA at 4°C overnight.

3. The tissues were washed with PBS at room temperature for 1 h, three times.
4. The tissues were decalcified in 350 mM EDTA-Na_2 (bring pH up to 6.5 using NaOH) at 37°C for 2–7 days depending on the age of the pigs, with a fresh buffer change every 24 h. All the incubation steps were performed with gentle shaking. After decalcification, the cochlea can be further separated from the bony structure via a bone cutter. For fetus cochlea, this step can be skipped since the cochlea can be extracted even before the decalcification step.
5. The decalcified tissues were dehydrated at room temperature with the methanol gradients (diluted in ddH_2O): 20% methanol for 2 h, 40% methanol for 2 h, 60% methanol for 2 h, 80% methanol for 2 h, and 100% methanol for 2 h twice.
6. The tissues were decolorized at 4 °C overnight with a mixture of 30% H_2O_2 and 100% methanol (v:v = 1:10).
7. The tissues were rehydrated at room temperature with the inverse methanol gradients (diluted in ddH_2O): 100% methanol for 2 h, 80% methanol for 2 h, 60% methanol for 2 h, 40% methanol for 2 h, 20% methanol for 2 h, and PBS for 2 h.
8. The tissues were permeabilized with PBS/0.2% Triton X-100/0.1% Deoxycholate/10% DMSO/25 mM EDTA (bring pH up to 6.5 using NaOH) at 37°C overnight.
9. The tissues were then blocked with PBS/0.2% Triton X-100/10% DMSO/5% normal donkey serum/25 mM EDTA (bring pH up to 6.5 using NaOH) at 37°C overnight.
10. The tissues were immunolabeled with the primary antibodies diluted (1:250) in PBS/0.2% Tween 20/10 μg/mL heparin/5% normal donkey serum/25 mM EDTA (bring pH up to 6.5 using NaOH) at 37°C for 5–7 days using immersion method or 2 days using a perfusion pump (Moatti et al., 2020).
11. The tissues were washed with PBS/0.2% Tween 20/10 μg/mL heparin/25 mM EDTA (bring pH up to 6.5 using NaOH) at 37°C for 24 h, with the fresh buffer, changed every 12 h.
12. The tissues were further immunolabeled with the secondary antibodies diluted (1:250) in PBS/0.2% Tween 20/10 μg/mL heparin/5% normal donkey serum/25 mM EDTA (bring pH up to 6.5 using NaOH) at 37°C for 5 days using the immersion method or 2 days using a perfusion pump.
13. The tissues were washed with PBS/0.2% Tween 20/10 μg/mL heparin/25 mM EDTA (bring pH up to 6.5 using NaOH) at 37°C for 48 h with the fresh buffer, changed every 12 h.
14. The tissues were dehydrated at room temperature with the methanol gradients (diluted in ddH2O): 20% methanol for 4 h, 40% methanol for 2 h, 60% methanol for 2 h, 80% methanol for 2 h, and 100% methanol for 2 h twice.
15. The tissues were then incubated at room temperature with the mixture of dichloromethane and methanol (v:v = 2:1) for 2 h twice, followed by 100% dichloromethane for 30 min four times.
16. The tissues were cleared at room temperature with 100% dibenzyl-ether (DBE) for 12–24 h, three times. All the incubation steps were performed with gentle shaking.

Custom-build light-sheet microscopy

A custom light-sheet microscope was utilized with three continuous-wave lasers (488 nm, 561 nm, and 640 nm; Coherent OBIS series). A detailed description of the setup is provided in our previous publications (Li et al., 2021a; Moatti et al., 2020; Rai et al., 2022). Briefly, for imaging the cochleae, a thin sheet of light is generated by scanning the Gaussian beam up and down across the field of view using the scanning galvo system. We have utilized the pivot galvo system to change the yaw and pitch angles of the illumination sheet of light to enable correction for deflections and obstructions in the passage of light through the complex bony structure of the cochlea while imaging. For big samples like porcine cochlea and deep in the tissue, slight variations in the index of refraction of the tissue versus the imaging media (DBE) changes the focal distance of the detection objective and prevents it from overlapping with the illumination beam, which leads to the blurriness of the acquired image. An additional degree of freedom that is the most important one when imaging the cochlea and improves the image quality tremendously is the ability to move the detection objective relative to the light-sheet position while imaging. This is adjusted when the illumination beam does not overlap with the focal plane of the detection objective during imaging deep into the tissue.

The specimen was mounted using a needle and placed in a custom chamber (aluminum and glass) to be immersed in dibenzyl ether (DBE). A silicone membrane was used to prevent damage to the detection objective lens when immersed in 100% DBE. The 10× detection objective had a numerical aperture of 0.6 (Olympus; XLPLN10XSVMP-2) and a working distance of 8 mm. The field of view of the microscope was ~1.7 mm^2.

QUANTIFICATION AND STATISTICAL ANALYSIS

Basilar membrane tracing

The acquired data was first stitched using TeraStitcher (Bria and Iannello, 2012), before being imported into IMARIS software (Oxford Instruments), and the associated voxel dimensions were set in the edit/image properties tab. We then used the "measurement points" tool under the "3D view" tab to assign points manually on the spiral trajectory of both the inner hair cells and outer hair cells along the organ of Corti from apex to base. For that purpose, two different tracings channels were used and the distance between points was ~50 μm. We then exported the 3D coordinate of points for further analysis into MATLAB. A total of 38 cochleae were traced: 4 cochleae were taken from E80 pigs, 15 cochleae were taken from P0 pigs, 6 cochleae were taken from P60 pigs, and 13 cochleae were taken from P120 pigs.

Hair cell length measurement

We extracted the cell length measurements from the 3D stitched images in IMARIS software using the "measurement points" tool under the "3D view" tab to assign points manually along the length of the hair cells (MYO7a channel). The measurement employed the "slice" view, where one can move between z-planes accurately and trace an individual hair cell that extends across multiple z-planes. The first point was assigned on top of the hair cell and moving back-and-forth between z-planes, a succession of points was assigned along the hair cell until the end of the hair cell was recognized (see Video S4). A line was fitted to the points, and its length represented the hair cell length.

Denoising

Partial maximum intensity projection (MIP) images were first generated for every 10–20 Z-planes. For each partial MIP, regions of interest were selected and segmented out in ImageJ using the brush tool. Afterward, an overall MIP was generated based on masked partial MIPs. For more details refer to (Moatti et al., 2020).

Hair cell counting

A semi-automated pipeline was utilized to count the number of inner hair cells from the obtained cochlea datasets. For more details please refer to our previous publication (Moatti et al., 2020). Briefly, the semi-automatic counting of IHCs and OHCs was performed with ilastik (Berg et al., 2019), version 1.3, and the automation was subjected to manual quality control. The outer hair cells were counted manually to remove the error generated due to the OHC elongation and presence of MYO7a throughout the cells' bodies. In this paper, hair cells from a total of 15 P0 cochleae were counted using the semi-automated pipeline.

Quantification of LGR5 expression

To quantify the LGR5 expression, the LGR5 intensity of 10 individual cells from each subset of supporting cells including GER, IBC, IPHC, IPC, OPC, DC12, DC3, and HS was measured via ImageJ and divided by the background intensity at 6 different frequencies. We divided the LGR5 intensity by the background to normalize the signal strength at different depths and positions, under the assumption that the background intensity i.e., autofluorescence should be equal in all locations in the organ of Corti for an individual sample (Greenbaum et al., 2017). A total of 16 cochleae (LGR5-H2B-GFP) were subject to quantification: 4 cochleae were taken from E80 pigs, 4 cochleae were taken from P0 pigs, 4 cochleae were taken from P60 pigs, and 4 cochleae were taken from P120 pigs.

Specifically, for each cochlea, 6 regions of interest (ROIs) were located based on their frequency. The supporting cells' structure followed a line drawn through aligned rows of cells in the high-resolution images of the cochlea, Figure S3. We have classified the supporting cells based on their relative position to the hair cells and each other as represented by separate lines in Figure S3. We have assigned cell identities starting from the top row as shown in Figure S3 with Hensen cells (HS). The HS line is a good reference point, as the HS express LGR5 constantly and independently of age and frequency. The next line structures to follow are Deiters cells (DC3, and DC12), pillar cells (PC), inner phalangeal cells (IPHC), inner border cells (IBC), and

inner sulcus cells (ISC) for mature cochleae or greater epithelial ridge cells (GER) for E80 cochleae. For each ROI, a circle background region (50 pixels in diameter) without any cells was selected using the oval selection tool in ImageJ. Ten regions that contained cells (7 pixels in diameter) were randomly selected for each assigned cell type in the region. The normalized expression of each cell was obtained by dividing the maximum intensity of each cell region by the average intensity of the background region. Once all regions were done, the intensity data were extracted and compiled into a GraphPad Prism file according to sample, region, and type of cell for analyses. This process was repeated for all cochleae. There are some cases where the relative intensity is below one. It occurs when the cell intensity is very low, and the large background patch includes some nonspecific antibody binding. Therefore, an intensity value equal to or below 1 indicates the absence of LGR5. (See Figure S3). The raw measurement data can be found at https://doi.org/10.17632/vdw3757cxv.1.

Control

As a control, in samples that have been simultaneously stained for MYO7a, the position of the supporting cell line structures should follow the organized structure of the hair cells. This is especially beneficial when the LGR5 expression was weak in certain supporting cell populations. Additionally, we have independently verified these observations by looking at cross-sections (or radial view), see Figure 6A. All in all, the organized line structure of the cells provided the framework to assign their identity.

Exclusion criteria

i) If the organized line structure was not clearly present in the LGR5 channel or the hair cells channel.

ii) If we could not identify a nucleus within the cells; LGR5 should be localized in the nucleus. All cells were selected only if we could recognize their nuclear shape.

iii) An area was excluded or replaced if the intensities were oversaturated or there was a major distortion such as the separation of the organ of Corti from the basilar membrane. In such situations, a slight move to the right or left was sufficient to find an area with a well-defined line based on hair cell organization.

vi) Given that different mounting orientations will result in variable surface view images, samples were excluded or reimaged, if their mounting orientation was drastically different.

STATISTICAL ANALYSIS

In the Results section, Figures 3, 4, 6, 7 and S1 legend, Table S1, and Table S2, the statistical analysis was performed using GraphPad Prism version 9.5. All the statistical details of the experiments can be found in the figure or table captions.

We used a one-way ANOVA, to investigate the effect of frequency/spatial positions on LGR5 expression at four ages (E80, P0, P60, and P120, N = 4, number of animals for each age). Ten measurements were made at each frequency (out of six) for seven cell types.

A mixed-effect model with correction for Tukey multiple comparison was used in Table S2. The age and frequency were selected as variables (N = 4, number of animals for each age). We have averaged ten measurement points per frequency and per cell type (six frequencies and seven cell types in total) from each cochlea. The four average numbers per cell type at each frequency and age were used as the input data.